Research Square

Preprints are preliminary reports that have not undergone peer review.
They should not be considered conclusive, used to inform clinical practice,
or referenced by the media as validated information.

Integration of microscopy and multi-omics data reveals pathology of a coral disease outbreak

Carly E. Karrick
University of California, Berkeley
Hannah L. Swain
The University of Texas at Arlington
Ashley M. Rossin
University of Miami
Mallory Kastner
Woods Hole Oceanographic Institution
Gillian Coleman
University of the Virgin Islands
Morgan Coleman
Texas A&M University – Corpus Christi
Lauren I. Howe-Kerr
Minderoo Foundation
Michelle A. Johnston
NOAA Office of National Marine Sanctuaries
Matthew D. Meyer
Rice University
Marissa F. Nuttall
NOAA Office of National Marine Sanctuaries
Mia K. Olson
Rice University
Amy Apprill
Woods Hole Oceanographic Institution
Marilyn Brandt
University of the Virgin Islands
Daniel M. Holstein
Stony Brook University
Laura Mydlarz
The University of Texas at Arlington
Adrienne M. S. Correa
amsc@berkeley.edu

University of California, Berkeley

Research Article

Keywords: amplicon sequencing, coral disease, coral immunity, gene expression, histopathology, holobiont, marine disease, metatranscriptomics, microbiome, multi-omics, symbiosis, transmission electron microscopy

Posted Date: August 19th, 2026

DOI: https://doi.org/10.21203/rs.3.rs-10349654/v1

License: This work is licensed under a Creative Commons Attribution 4.0 International License. Read Full License

Additional Declarations: No competing interests reported.

Integration of microscopy and multi-omics data reveals pathology of a coral disease outbreak

Carly E. Karrick[1,2]*, Hannah L. Swain[3]*, Ashley M. Rossin[4,5], Mallory Kastner[6,7], Gillian Coleman[5,8], Morgan Coleman[5, 9], Lauren I. Howe-Kerr[2,10], Michelle A. Johnston[11], Matthew D. Meyer[12], Marissa F. Nuttall[11], Mia K. Olson[2], Amy Apprill[6], Marilyn Brandt[8], Daniel M. Holstein[5,13], Laura Mydlarz[3], Adrienne M.S. Correa[1,2]

[1]Department of Environmental Science, Policy, and Management, University of California, Berkeley, CA, USA
[2]Biosciences Department, Rice University, Houston, TX, USA
[3]Department of Biology, The University of Texas at Arlington, TX, USA
[4]Cooperative Institute for Marine & Atmospheric Studies, University of Miami, FL, USA
[5]Department of Oceanography & Coastal Sciences, Louisiana State University, Baton Rouge, LA, USA
[6]Department of Marine Chemistry and Geochemistry, Woods Hole Oceanographic Institution, Woods Hole, MA, USA
[7]MIT-WHOI Joint Program in Oceanography/Applied Ocean Science and Engineering, Earth, Atmospheric and Planetary Sciences, Cambridge and Woods Hole, MA, USA
[8]Center for Marine and Environmental Studies, University of the Virgin Islands, USVI, USA
[9]Harte Research Institute, Texas A&M University-Corpus Christi, Corpus Christi, TX, USA
[10]Minderoo Foundation, Perth, WA, Australia
[11]National Oceanic and Atmospheric Administration (NOAA) Office of National Marine Sanctuaries, Flower Garden Banks National Marine Sanctuary, Galveston, TX, United States,
[12]Shared Equipment Authority, Rice University, Houston, TX, USA
[13]School of Marine and Atmospheric Sciences, Stony Brook University, Stony Brook, NY, USA

*Co-first authors

Corresponding author: Adrienne M.S. Correa (amsc@berkeley.edu)

Abstract

Background: Marine disease outbreaks are increasing in frequency and severity, threatening coral reef function and persistence. Coral diseases are often difficult to distinguish due to similar gross pathology and frequently unresolved etiologies. Integrating diverse data types (e.g., morphology, molecular, and microbial) may clarify disease etiology, yet few marine studies have integrated them. In August 2022, a multi-species coral disease outbreak with pathology consistent with white syndromes (stony coral tissue loss disease and white plague) occurred at the Flower Garden Banks (northwest Gulf of Mexico). To characterize this disease, we combined microscopy (histopathology and transmission electron microscopy) with multi-omics approaches

(comparative metatranscriptomics; 16S rRNA gene sequencing, and Symbiodiniaceae ITS-2 sequencing) to 15 apparently healthy and diseased *Pseudodiploria strigosa* corals collected during the initial outbreak.
Results: Analysis revealed signatures of pathology, including coral-Symbiodiniaceae dysbiosis characterized by shrunken Symbiodiniaceae cells and vacuoles, coral and Symbiodiniaceae gene expression indicative of immune stress, and the presence of putative viral structures. Integrating these data types provided a more comprehensive view of disease dynamics within the coral holobiont by linking histopathological changes with molecular signatures of immune response, nutrient deficiency, coral-Symbiodiniaceae dysbiosis, and enrichment of a viral operational taxonomic unit (Order Orthopolintovirales).
Conclusions: Combined evidence from morphology, reef monitoring, pathology, and comparison with stony coral tissue loss disease identified the outbreak as white plague. We present the first descriptions of white plague in *P. strigosa* across multiple data types. This study provides an integrative framework for characterizing marine diseases across cellular, sub-cellular, microbial, viral, and transcriptomic scales.

Key words
amplicon sequencing, coral disease, coral immunity, gene expression, histopathology, holobiont, marine disease, metatranscriptomics, microbiome, multi-omics, symbiosis, transmission electron microscopy

Background

Across marine ecosystems, disease prevalence is increasing in frequency and severity as sea surface temperatures rise [1]. Effective identification and management of marine disease is imperative because disease outbreaks can spur rapid and widespread mortality, with cascading ecosystem-level decline [2]. However, marine disease etiologies can be elusive. For example, it can be challenging to: (1) fulfill Koch's postulates due to difficulty establishing cultures of marine microbes [3]; (2) parse causative agents vs. secondary/opportunistic infections [4]; and (3) sample when diseases first establish, since sampling is typically based on visible lesions that often develop in later stages of disease progression (e.g., [5]). These challenges are especially pronounced for reef-building corals, where white syndromes such as white plague (WP) and stony coral tissue loss disease (SCTLD) are characterized by similar macroscale pathologies, affect multiple species, and are likely influenced by polymicrobial consortia [6–8]. Despite these challenges, several tools are available to clarify coral disease pathology and etiology, including gross morphology, microscopy/histopathology, and molecular analyses of microbial communities and holobiont gene expression. Although integrating these tools to characterize a set of diseased and apparently healthy individuals will more holistically characterize coral diseases, only one to two methodologies are typically applied in a given study.

WP and SCTLD are characterized by lesions with tissue loss that spread across a coral colony [9] and a combination of recent studies employing a range of diagnostic tools have yielded insights about their etiologies. SCTLD has received significantly more research attention than WP over the last decade (Supplemental File 1: Table 1), so SCTLD etiology has more robust evidence and some foundational WP studies were conducted prior to the development of advanced high-throughput sequencing technology and statistical software packages. Overall, WP is thought to be caused by polymicrobial dysbiosis [9], whereas SCTLD is hypothesized to be a breakdown in the coral-Symbiodiniaceae symbiosis [10–12]. In WP, microbes and viruses are hypothesized to play an etiologic role. Metagenomic and metatranscriptomic evidence suggests WP-affected corals harbor distinct viruses compared to healthy corals, which is supported by the presence of virus-like particles in WP-affected tissues [13,14]. The proliferation of some bacteriophages in WP-affected tissues has been correlated with opportunistic infection of cyanobacteria and *Pantoea* bacteria [13]. Differential tolerance to bacterial dysbiosis has also been associated with WP resistance among coral species, where WP-resistant coral species have higher dysbiosis thresholds [15]. Coral gene expression profiles also mediate WP phenotype, with certain genes associated with diseased vs. healthy tissues and resistant/resilient individuals/species vs. more susceptible ones [13,16].

Microscopy and molecular signatures of SCTLD suggest it results in coral-Symbiodiniaceae dysbiosis as the lesion spreads from the basal body wall, the Symbiodiniaceae:vacuole ratio increases, and tissue sloughs off [5,11]. An early hypothesis was that SCTLD is caused by a Symbiodiniaceae-infecting virus, supported by the presence of filamentous virus-like particles in electron micrographs of Symbiodiniaceae from SCTLD-affected tissues ([12], but see [17]), evidence of differential susceptibility to SCTLD among Symbiodiniaceae lineages [18–22], and upregulation of the symbiophagy gene *Rab7* in SCTLD-affected corals [10]. Alternatively, opportunistic viral infection may more indirectly contribute to SCTLD signs since various viral lineages – including bacteriophage and putative coral- and Symbiodiniaceae-infecting viruses – were enriched in diseased tissues of corals experimentally exposed to SCTLD [23]. Opportunistic infections may involve bacteria, as antibiotic treatment has been shown to halt SCTLD lesion progression (but not prevent the formation of new lesions; [24]) and certain bacterial groups are more abundant adjacent to disease lesions relative to apparently healthy tissue [25,26]. While these studies characterizing WP and SCTLD are useful, some of their findings cannot be directly compared: some holobiont members are only examined or data types are only available for one disease (and not the other), and the studies originated from different biogeographic regions and coral species.

Here, we capitalize on what has become a relatively unique opportunity - to study coral disease on a historically low-disturbance reef [27]. Flower Garden Banks (FGB) in the northwest Gulf of Mexico is a high–coral cover ecosystem dominated by reef-building species extending to 46 m depth [28]. Due to the remoteness, oceanographic connectivity and depth range, FGB has

exhibited historically low coral disease prevalence [27,28]; WP-like signs have only occasionally been documented in FGB corals [29–31]. Yet, in August 2022, an unidentified multi-species coral tissue loss disease emerged on the FGB [32]. It is possible that the disease was spread via an extended phase of the Loop Current that connects the Caribbean Sea to the Gulf of Mexico [27]. Multiple scleractinian coral species were impacted, with the highest initial prevalence in *Pseudodiploria strigosa* [32]. Initial disease management efforts included use of a silicone-based paste called Base2B (Ocean Alchemists LLC) mixed with amoxicillin trihydrate applied to lesions and subsequently monitored in 6-month intervals [32]. The disease remained active in March 2023, but corals had largely recovered by July 2024, when very low coral mortality was observed. Continued disease monitoring and preliminary histology analyses, alleviated concern that the disease was SCTLD [33]. However, because the lesions exhibited pathology resembling white syndromes such as SCTLD and WP, further characterization of this disease is critical to inform management strategies and guide future efforts.

Here, we use an uncommonly comprehensive approach to characterize coral disease by applying multiple tools to the same samples to integratively describe a disease. We combine microscopy and molecular-based 'omics sequencing methods to study disease-associated: (1) cell-level histopathology (light microscopy); (2) ultrastructural-scale evidence of Symbiodiniaceae degradation and/or viral infection (TEM); (3) microbial community composition - bacteria/archaea (16S rRNA gene amplicon sequencing), Symbiodiniaceae (internal transcribed spacer-2 (ITS-2) amplicon sequencing), and viruses (metatranscriptomics); and (4) differentially expressed genes in coral/Symbiodiniaceae (metatranscriptomics). We then integrate across these diverse data types using gene expression networks and correlate viral lineages to disease phenotypes identified through TEM and histopathology. We apply these approaches to healthy and diseased *Pseudodiploria strigosa* corals collected in FGB in September 2022, following initial signs of disease and before antibiotic treatment (Figures 1-2). We highlight unique microbial features and gene expression profiles characteristic of the disease. In doing so, we demonstrate the importance and efficacy of our comprehensive approach to studying coral disease, as we are able to characterize this disease as WP (and not SCTLD). As such, our results constitute the first description of WP in *P. strigosa* corals.

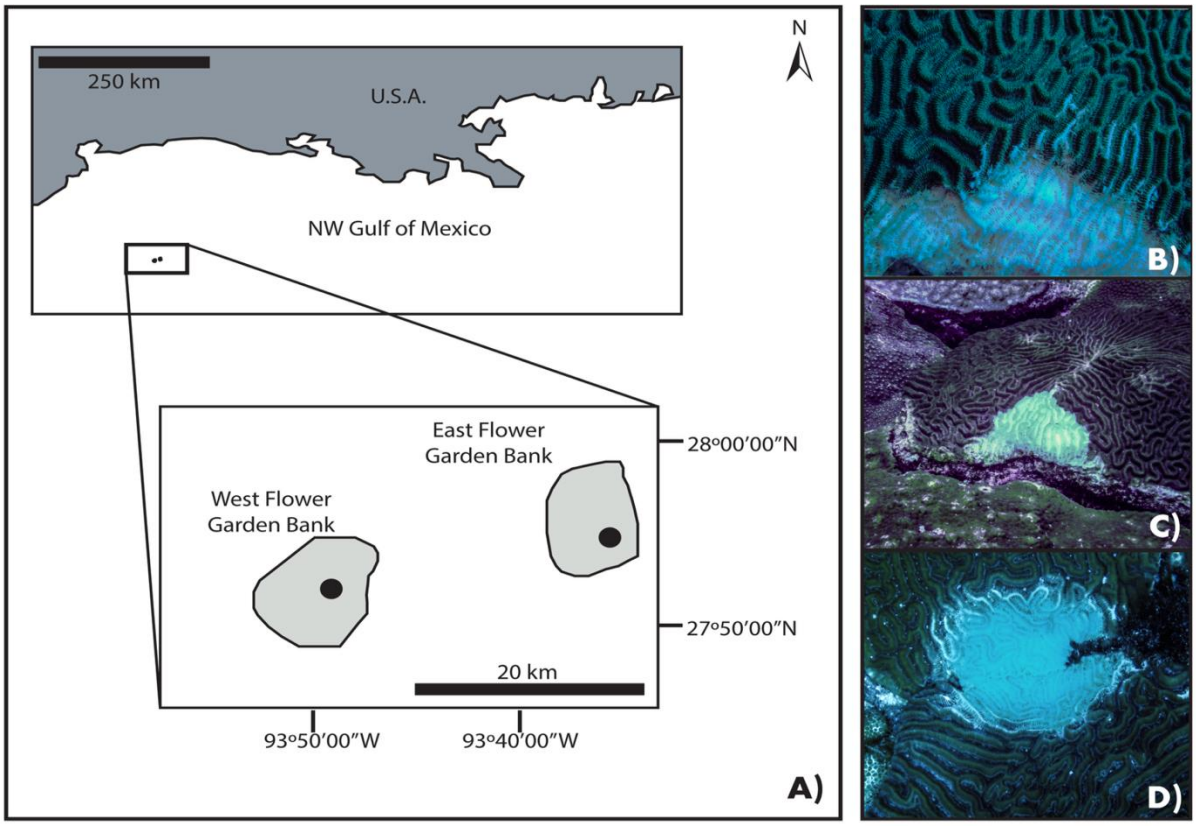


Figure 1: A) Map of the Flower Garden Banks National Marine Sanctuary. The inset map represents two sampling sites: West Bank and East Bank. Buoys are noted by circles. **B-D)** Representative images of disease on sampled *P. strigosa* colonies. Map adapted from Maher et al. (2018).

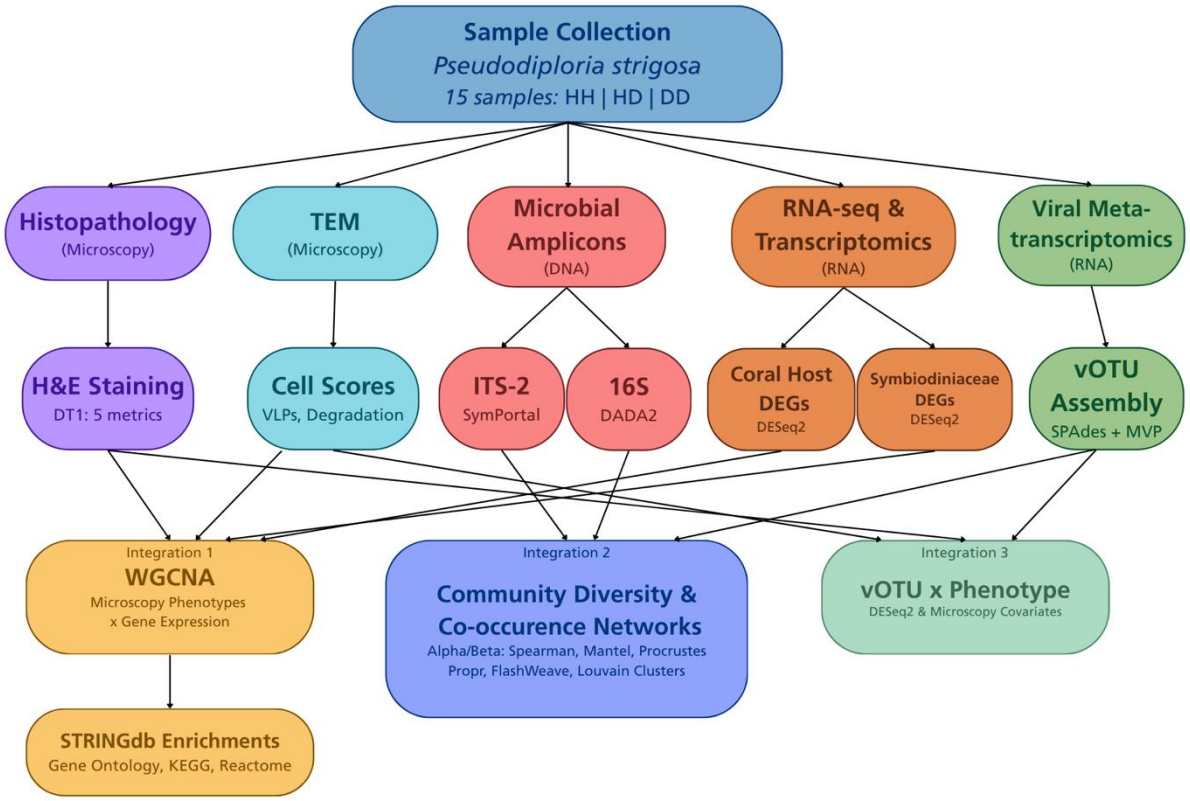


Figure 2: Integrative multi-omics and microscopy framework for assessing coral holobiont disease in *Pseudodiploria strigosa.* HH: apparently healthy tissue on an apparently healthy coral; HD: apparently healthy tissue on a diseased coral; DD: lesion-adjacent tissue; TEM: transmission electron microscopy; DEG: differentially expressed gene; vOTU: viral operational taxonomic unit; WGCNA: weighted gene co-expression network analysis.

Results

Our overall results indicated that relative to apparently healthy conspecifics, diseased corals exhibited various abnormal characteristics (Table 1), including histopathological differences indicative of disease-driven abnormalities rather than tissue loss via predation. The often multi-focal lesions of *P. strigosa* [32] were characterized by shrunken Symbiodiniaceae cells and vacuoles housing them (Table 1), which was correlated with transcriptional shifts and altered Symbiodiniaceae cell ultrastructure. Below, we provide detailed results from each analytical approach and the integration of analyses, including comparisons between apparently healthy tissue on apparently healthy corals (HH) and both lesion-adjacent (DD) and apparently healthy tissue (HD) on diseased corals.

Major Finding	Supporting Data Type / Result

Coral host mounts an immune response to the disease via protein degradation, autophagy and cell degradation	***Histopathology***
	Shrunken Symbiodiniaceae and vacuole area in diseased corals (HD, DD) relative to apparently healthy corals (HH).
	Host gene expression
	Highest magnitude of immune response and early signs of disease indicated in apparently healthy tissue of diseased coral relative to apparently healthy tissue from a healthy coral.
Putative viral structures and abnormal gene expression in Symbiodiniaceae of diseased corals	***TEM***
	Greater proportion of Symbiodiniaceae cells with multi-membrane vesicles adjacent to disease lesions compared to apparently healthy tissue. Greater proportion of Symbiodiniaceae cells with putative spherical/icosahedral virus-like particles and starch granules in diseased corals relative to apparently healthy corals.
	Symbiodiniaceae gene expression
	Symbiodinaceae in diseased tissue are shifting to a stressed, low-metabolic state while activating cyto-skeletal activity in response to early-signs of dysbiosis.
Bacteria, Archaea, Symbiodiniaceaeand viruses may not play a major etiologic role in the FGBNMS disease	***Bacteria and Archaea 16S rRNA gene***
	No uniformity within the *P. strigosa* archaeal/bacterial communities across all health types. Bacteria and archaea communities in all health states appear dysbiotic compared with healthy corals in other species and regions.
	Symbiodinaceae ITS-2
	Consistent ITS-2 type profile composition across health states. All samples dominated by one of five *Breviolum* ITS-2 type profiles with dominant defining intragenomic variant (DIV) B1.
	Viruses vOTU

	No partitioning of overall vOTU alpha or beta diversity by health state. Increased abundance of two bacteriophage vOTUs in apparently healthy corals relative to diseased corals, but no differential abundance of eukaryotic viruses.
Statistical power too low to assess cross-Domain microbial associations	***Bacteria and Archaea:Viruses***
	No correlations between archaeal/bacterial and viral alpha or beta diversity. Statistical power too low to assess proportional relationships and co-occurrence networks.
	Symbiodinaceae:Viruses
	No correlations between Symbiodiniaceae and viral alpha or beta diversity. Statistical power too low to assess proportional relationships and co-occurrence networks.
Evidence of coral-Symbiodiniaceae dysbiosis and nutrient deficiency in diseased corals	***Histopathology:Host gene expression***
	Shrinkage of Symbiodiniaceae -housing vacuole linked to protein binding, SNARE activity and serine-endopeptidase activity
	Histopathology:Symbiodiniaceae gene expression
	Shrinkage of Symbiodiniaceae cells linked to metabolic processes, endocytosis and cellular response to stress.
	TEM:Symbiodiniaceae gene expression
	Genes associated with increase of starch granules in diseased tissues are enriched for pathways involved in lipid, fatty acid and carbohydrate metabolism.
	Histopathology:Viruses
	vOTU (Order Pimascoviraless) was significantly more abundant in samples with larger Symbiodiniaceae and vacuole areas. vOTU (Order Orthopolintovirales) had the opposite pattern.

174 **Table 1:** A summary of this study's major findings and the associated datasets/results that
175 support those findings that support the characterization of White Plague disease. Datasets include
176 light microscopy (histopathology), transmission electron microscopy (TEM), composition of
177 amplicon sequence variants (ASVs) generated from sequencing of the v4 region of the 16S

rRNA gene, composition of Symbiodiniaceae ITS-2 type profiles generated from sequencing of the internal transcribed spacer-2 (ITS-2) region of Symbiodiniaceae rDNA, host (*Pseudodiploria strigosa* corals) gene expression isolated from bulk RNA-Seq data, Symbiodiniaceae (dominant genus *Breviolum*) gene expression isolated from bulk RNA-Seq data, and composition of virus operational taxonomic units (vOTUs) mined from bulk RNA-Seq data. Samples were collected from coral tissue of various health states, where HH: apparently healthy tissue on an apparently healthy coral; HD: apparently healthy tissue on a diseased coral; DD: lesion-adjacent tissue.

Quantitative histopathology

Average Symbiodiniaceae area ($p = 0.0248$) and average vacuole area ($p = 0.0115$, Figure 3, Figure 4 B,H) were significantly different between health states. Average Symbiodiniaceae area for HH samples was 29.72 ± 2.72 µm, HD was 26.05 ± 1.92 µm, and DD was 25.33 ± 2.19 µm. A one-way ANOVA and Tukey post-hoc test revealed that DD samples had significantly smaller average Symbiodiniaceae area compared to HH samples ($p = 0.029$), while there were no significant differences between HD and HH ($p = 0.068$) or between DD and HD ($p = 0.878$). Average vacuole area for HH samples was 54.0 ± 3.98 µm, HD was 47.8 ± 3.13 µm, and DD was 47.3 ± 2.5 µm. A one-way ANOVA with Tukey post-hoc test revealed that average vacuole area differed significantly by health state. Both HD and DD samples had significantly smaller vacuole areas compared to HH samples ($p = 0.027$). No significant difference was detected between DD and HD samples ($p = 0.017$). Overall, Symbiodiniaceae and vacuoles were smaller in diseased samples than healthy samples.

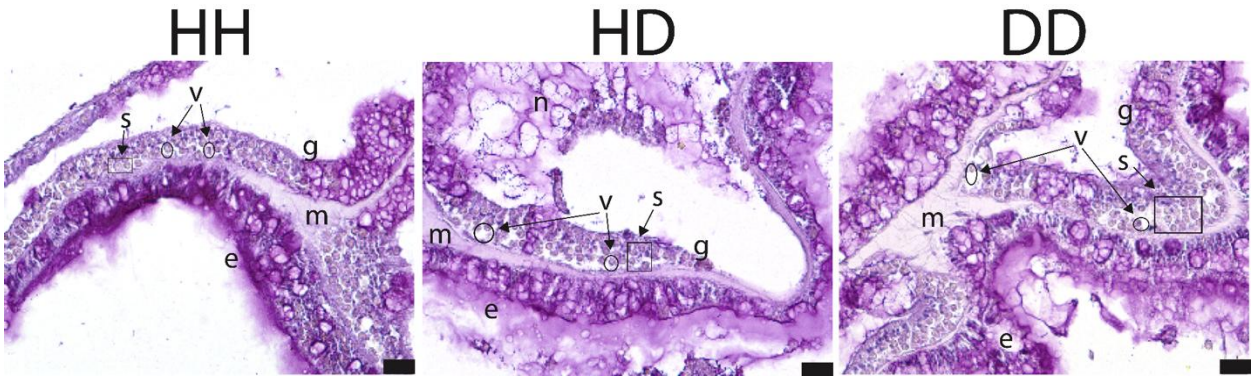


Figure 3: Histological pictographs of apparently healthy tissue from apparently healthy colony (HH), apparently healthy tissue from disease colony (HD), and diseased tissue from diseased colony (DD) tissues. Black scale bars are 50 µm. Symbols are denoted as follows: e: epidermis, m: mesoglea, g: gastrodermis, s: algal symbionts, square surrounds smaller and degraded symbionts, v: vacuolization, oval surrounds symbionts with larger vacuoles.

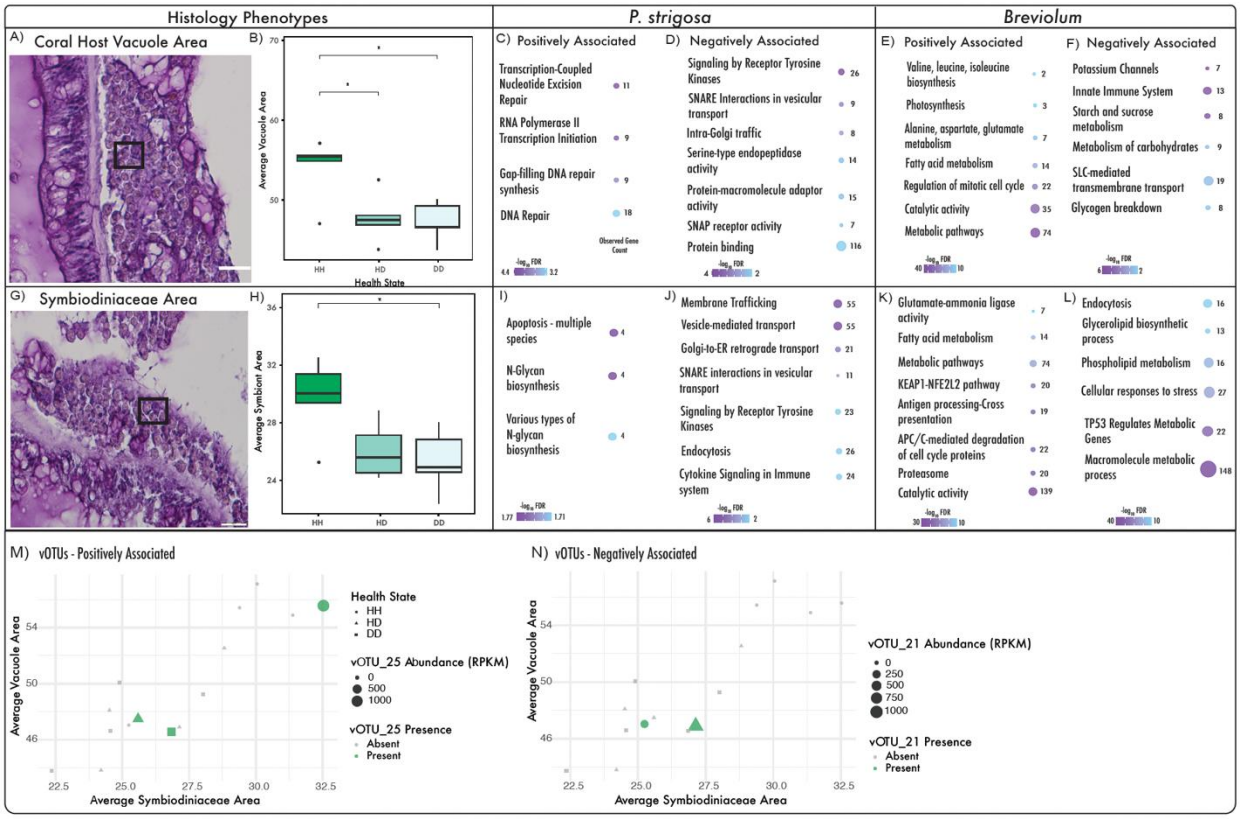


Figure 4: A–F: Integration of histopathology, coral host, and Symbiodiniaceae gene expression showing vacuole (symbiosome) shrinkage in diseased coral tissue. (A) Representative histopathology image of shrinking vacuoles in diseased colonies (DD). (B) Boxplot showing reduced vacuole area in HD and DD colonies. (C–F) Coral host (C–D) and Symbiodiniaceae (E–F) functional enrichment GO terms from WGCNA and STRING DB positively (C, E) and negatively (D, F) associated with average vacuole area. G–L: Integration of histopathology, coral host, and Symbiodiniaceae gene expression showing Symbiodiniaceae shrinkage in diseased coral tissue. (G) Representative histopathology image of shrinking Symbiodiniaceae in DD colonies. (H) Boxplot showing reduced Symbiodiniaceae area in HD and DD colonies. (I–L) Dominant Symbiodiniaceae (*Breviolum*) (I–J) and total Symbiodiniaceae (K–L) GO terms positively (I, K) and negatively (J, L) associated with average Symbiodiniaceae area. M-N) Average Symbiodiniaceae and vacuole area for viral operational taxonomic units (vOTUs) significantly positively (vOTU_25; M) and negatively (vOTU_21; N) associated with these features based on DESeq analyses. In panels M and N, icon size indicates vOTU abundance based on RPKM values, shape indicates health state, and color indicates presence/absence of a vOTU in a sample. Health states are abbreviated for: HH: apparently healthy tissue on an apparently healthy coral; HD: apparently healthy tissue on a diseased coral; DD: lesion-adjacent tissue.

Transmission electron microscopy (TEM) of Symbiodiniaceae cells

Notably, three types of structures were identified as associated with the disease: multi-membrane vesicles (MMVs), spherical/icosahedral virus-like particles (VLPs), and starch granules. MMVs were highly ordered spherical or semi-spherical bodies of concentric electron-dense rings with an average diameter of 293 nm, ranging from 122 to 549 nm (Figure 5 A-B). Single spherical/icosahedral VLPs were identified as small, spherical or icosahedral particles ranging from 41 to 910 nm in diameter, with an average diameter of 131 nm (Figure 5 C-D). These VLPs were primarily observed as individual particles, with crystalline arrays of spherical/icosahedral VLPs observed in two cells, and were found in chloroplasts in ~41.2% (47 of 114) cells containing these particles. Floridean starch granules were observed as semi-spherical electron-lucent features observed in the cytoplasm (Figure 5 E-F).

Some putative viral structures and cell abnormalities were associated with diseased health states based on TEM analyses (Supplemental File 1: Table 2). MMVs were present in ~3.4% (4 of 119) of HH cells, ~3.7% (5 of 136) of HD cells, and ~17.4% (30 of 172) of DD cells. The proportion of cells with MMVs significantly varied across health states ($\chi^2 = 23.93$, $p = 6.36 \times 10^{-6}$; ANOVA of binomial logistic regression; Supplemental File 2: Figure 1), with significant enrichment in DD tissues compared to other health states (HH - DD contrast, $p = 0.0028$; HD - DD contrast, $p = 0.0017$). The presence of MMVs was significantly positively correlated with large cavities ($r = 0.2498$, $p = 1.698 \times 10^{-7}$) and significantly negatively correlated with indistinct thylakoid membranes ($r = -0.1431$, $p = 0.003038$) (Supplemental File 2: Figure 2).

Spherical/icosahedral VLPs were present in ~8.4% (10 of 119) of HH cells, ~28.7% (39 of 136) of HD cells, and ~25.6% (44 of 172) of DD cells. The proportion of cells with spherical/icosahedral VLPs significantly varied across health states ($\chi^2 = 20.32$, $p = 3.865 \times 10^{-6}$; ANOVA of binomial logistic regression; Supplemental File 2: Figure 1), with significantly fewer in HH tissues (HH - HD contrast, $p = 0.0003$; HH - DD contrast, $p = 0.0012$). The presence of spherical/icosahedral VLPs was also significantly negatively correlated with indistinct organelles ($r = -0.1071$, $p = 0.02686$) and abnormal membranes ($r = -0.1196$, $p = 0.0134$) (Supplemental File 2: Figure 3).

Starch granules (Figure 5 E-F) were present in ~73.9% (88 of 119) of HH cells, ~73.5% (100 of 136) of HD cells, and ~85.5% (147 of 172) of DD cells, with significant variation across health states in the proportion of cells with starch granules ($\chi^2 = 8.702$, $p = 0.01289$; ANOVA of binomial logistic regression; Figure 6A). DD tissues had a significantly greater proportion of cells with starch granules compared to other health states (HH - DD contrast, $p = 0.0409$; HD-DD contrast, $p = 0.0268$). The presence of starch granules was significantly negatively correlated with assessed characteristics of Symbiodiniaceae cell degradation, including indistinct organelles ($r = -0.2400$, $p = 5.205 \times 10^{-7}$), an abnormal cell membrane ($r = -0.3192$, $p = 1.426 \times 10^{-11}$), indistinct thylakoid membranes ($r = -0.2044$, $p = 2.079 \times 10^{-5}$), absence of the pyrenoid body ($r = -0.1788$, $p = 2.050 \times 10^{-4}$), and overall degradation ($r = -0.2083$, $p = 1.425 \times 10^{-5}$) (Supplemental

File 3: Figure 4). The proportion of cells with the other putative viral structures and cell abnormalities assessed did not significantly vary between health states (Supplemental File 1: Table 2).

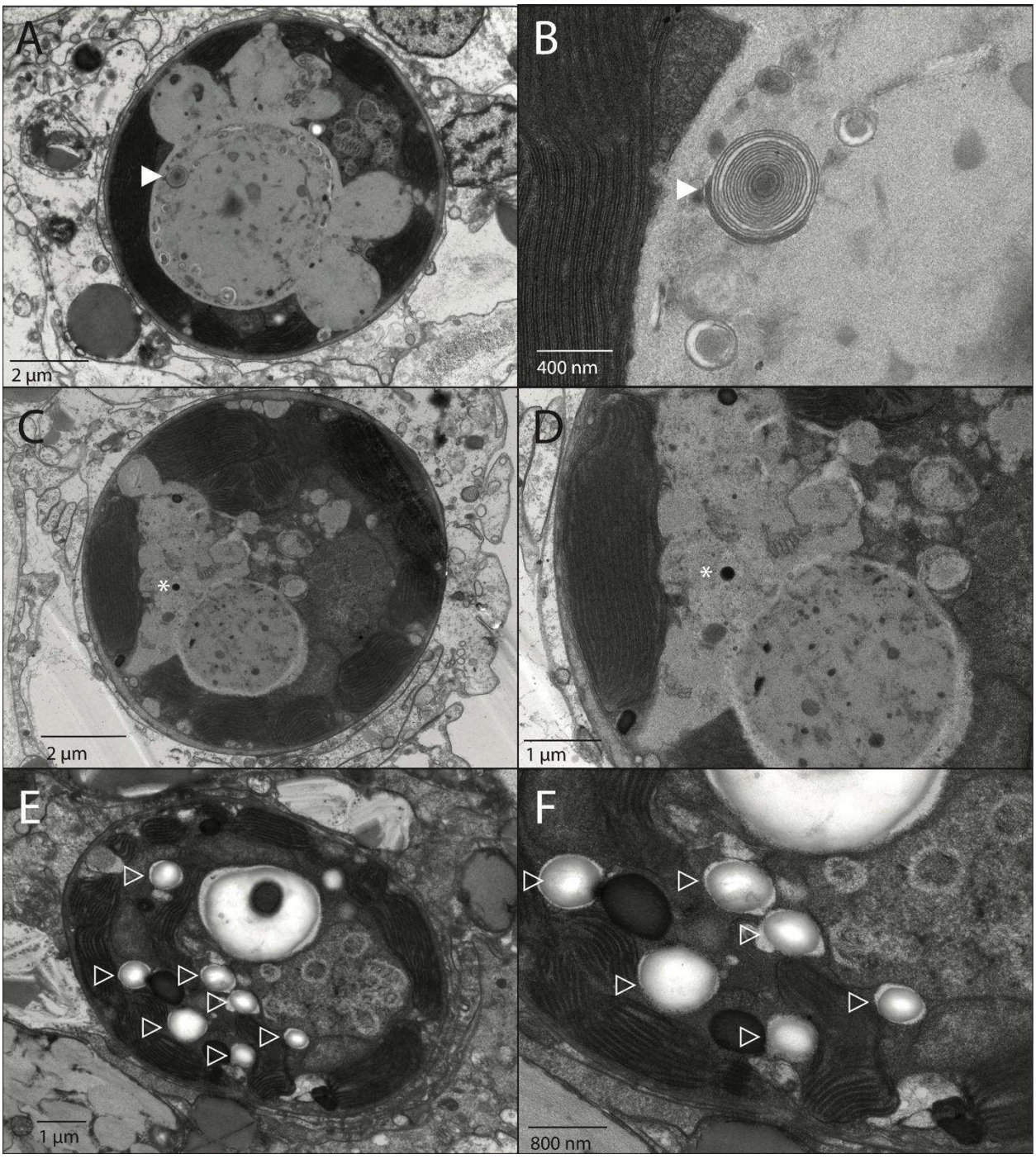


Figure 5: Representative TEM images of multi-membrane vesicles from lesion-adjacent tissues (A, B), spherical/icosahedral virus-like particles from apparently healthy tissue on a diseased coral (HD) (C, D), and starch granules from HD tissues (E, F). Filled white arrowheads indicate multi-membrane vesicles (A, B), asterisks indicate spherical/icosahedral virus-like particles (C,

D), and empty arrowheads indicate starch granules (E, F). In order from A to F, scale bars are 2 µm, 400 nm, 2 µm, 1 µm, 1 µm, and 800 nm.

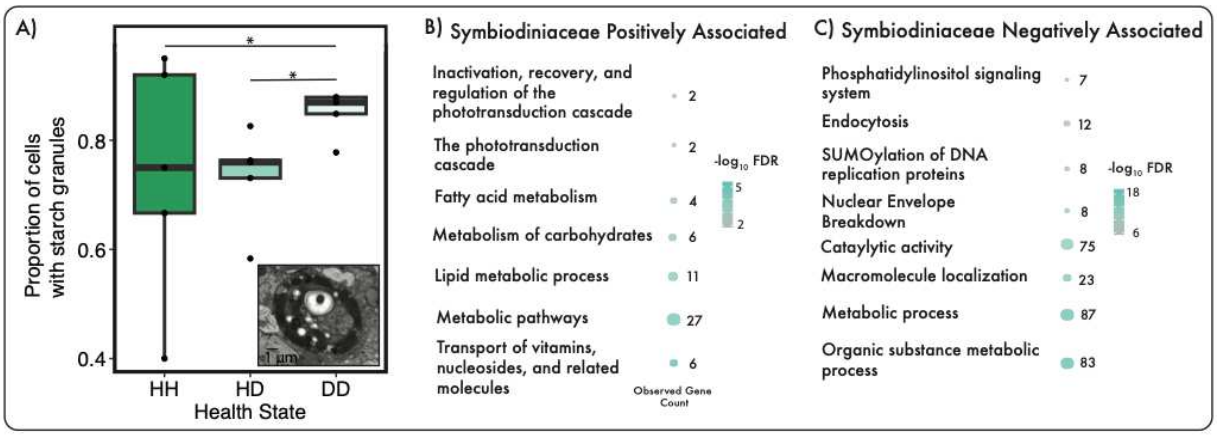


Figure 6: Proportion of cells with starch granules across health states (A) and Symbiodiniaceae gene functional modules positively (B) and negatively (C) associated with the proportion of cells with starch granules. DD tissues have a significantly higher proportion of Symbiodiniaceae cells with starch granules compared to HH and HD tissues (A). The inset of (A) shows a representative cell with starch granules (scale bar: 1 µm). Health states are abbreviated for: HH: apparently healthy tissue on an apparently healthy coral; HD: apparently healthy tissue on a diseased coral; DD: lesion-adjacent tissue.

Symbiodiniaceae composition (ITS-2)

An average of 11,480 ITS-2 reads were recovered per sample; the range of reads per sample was 461 to 40,225 (Supplemental File 1: Table 3). Six total Symbiodiniaceae ITS-2 type profiles were detected, five in the genus *Breviolum* (dominant DIV B1) and one in the genus *Symbiodinium* (A2b) (Figure 7A). All samples were dominated by one of the five *Breviolum* lineages, and BBsplit analysis corroborated *Breviolum* as the dominant Symbiodiniaceae genus (Figure 7A). *Symbiodinium* A2b was present at ~0.17% abundance in one sample (003_DD). Symbiodiniaceae ITS-2 sequence beta diversity did not vary between tissue health states according to a PERMANOVA test (df = 2, SumOfSqs = 0.6667, R^2 = 0.13699, F = 0.9524, p = 0.488). Most sample pairs (0.6%, 3 of 5) from individual diseased corals contained the same Symbiodiniaceae ITS-2 type profile in their DD and HD tissues, but HD and DD tissues from corals 003 and 005 differed (Figure 7A).

Coral de novo *transcriptome assembly and annotation*

The assembled de novo transcriptome had a total of 14,424 transcripts. The BUSCO score was 69.10% (n = 954), with an N50 of 3635 (Supplemental File 1: Table 4). Annotation of the transcriptome with NCBI's Uniprot database resulted in 75% of the transcripts in the transcriptome having annotations.

Differentially expressed genes of coral host and Symbiodiniaceae

In *P. strigosa,* the DESeq2 analysis identified 35 differentially expressed genes (DEGs) in HH vs HD, 12 DEGs in HH vs DD and 6 DEGs in HD vs DD. In *Breviolum,* the DESeq2 analysis identified 3 DEGs in HH vs HD, 5 DEGs on HH vs DD and 1 DEG in HD vs DD (Figure 7 B-F). Both analyses had a large log 2 Fold Change (-27 to 21 L2FC), resulting in high variation across samples, leading to a low number of DEGs (Supplemental File 2: Figure 5). The principal component analysis performed did not identify clustering by sample health state; no outliers were detected in the dataset (Supplemental File 2: Figure 6). HH vs HD in *P. strigosa* had the highest amount of DEGs with a total of 35. These DEGs display expression patterns of upregulation of protein degradation, recycling, autophagy and an anti-inflammatory response in the HD portion of the diseased colony. The majority of DEGs identified in the dominant Symbiodiniaceae genus (*Breviolum)* lack annotations (Figure 7 G-K); only three were annotated. *Axonemal dynein light intermediate polypeptide 1* was upregulated in DD tissue, whereas *small ribosomal subunit protein* and *large ribosomal subunit protein* were down regulated in DD tissue.

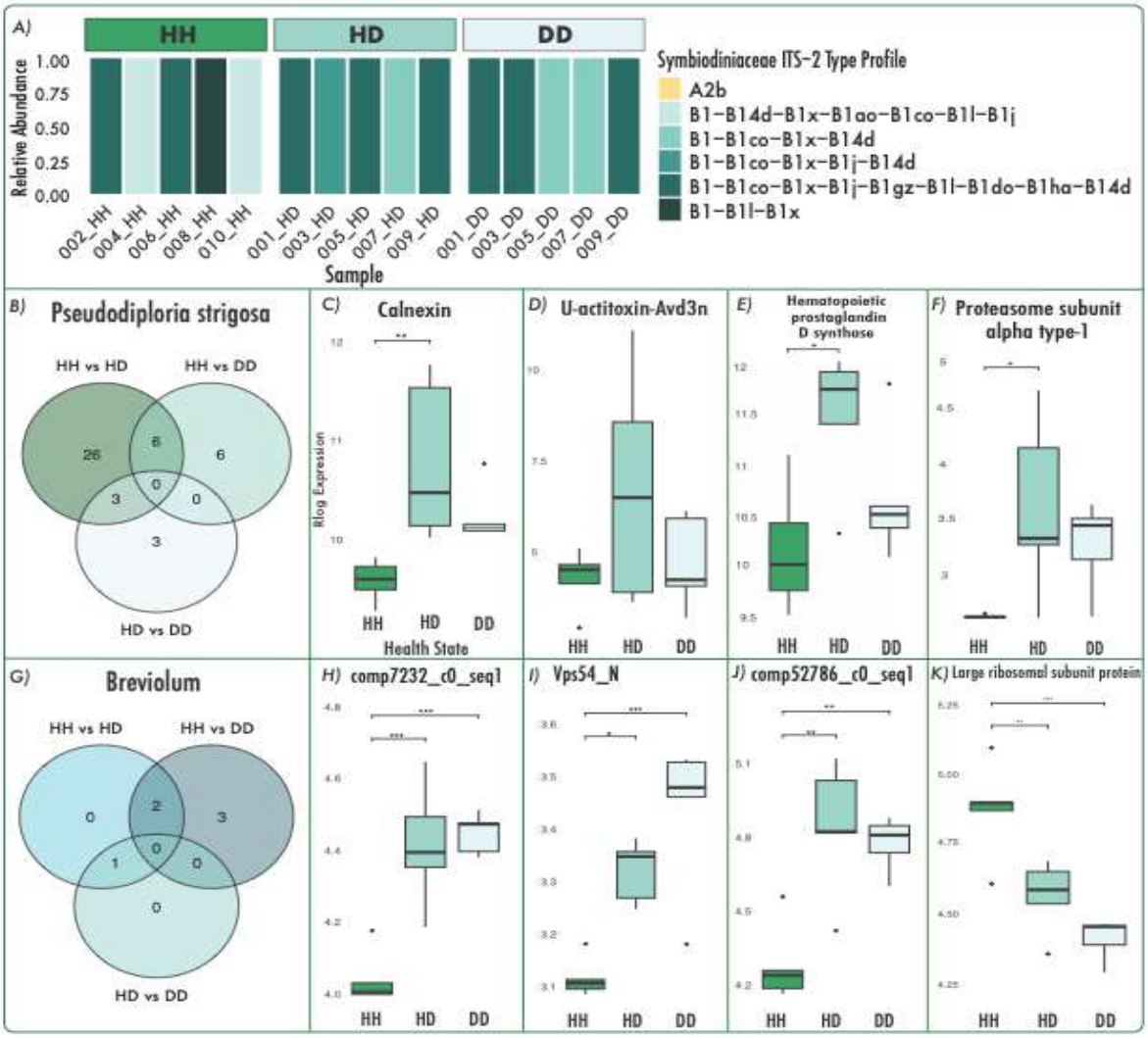


Figure 7: Per-sample Symbiodiniaceae composition based on internal transcribed spacer-2 (ITS-2) rDNA (A). Bolded sample names on the x-axis indicate samples with different dominant ITS-2 type profiles across health states in (A). Differentially expressed genes (DEGs) across health states in the coral host (B-F) and dominant Symbiodiniaceae genus (G-K). Coral host DEGs are from the contrast argument HH vs HD, displaying a significant increase in expression in the HD health state. Symbiodiniaceae DEGs are from the contrast argument HH vs DD. Health states are abbreviated for: HH: apparently healthy tissue on an apparently healthy coral; HD: apparently healthy tissue on a diseased coral; DD: lesion-adjacent tissue.

Bacteria/archaea composition (16S rRNA gene)

A total of 5,198,662 total bacterial/archaeal 16S rRNA gene reads were sequenced (54,581 to 201,598 reads per sample; average = 109,713 reads, standard deviation = 35,637 reads). After removing two samples from coral 007 that were mislabelled during sample processing and ASVs with zero abundance, those associated with mitochondria and chloroplasts, and those from

controls, 4,705 ASVs remained over 13 samples (110 to 1,129 ASVs per sample; average = 399 ASVs; standard deviation = 323 ASVs). Bacterial/archaeal beta diversity was not significantly different by tissue health state (PERMANOVA: $p = 0.302$, $R^2 = 0.16914$) (Supplemental File 2: Figure 7). SIMPER analysis identified the following average similarity percentages per health states: 9.78% for HH, 6.52% for HD and 8.79% for DD (Supplemental File 1: Table 4). Among the three differential abundance analyses, only ASV1 (*Pseudovibrio denitrificans*) was identified as differentially abundant between HD and DD (depleted in DD). Moreover, no pronounced core bacterial/archaeal microbiome was detected within or across tissue states, suggesting low consistency in ASVs across samples. Only HH samples associated with ASV11 (*Synechococcus* CC9902), and it was present in >80% of HH samples with a relative abundance greater than 0.05%. Overall, no uniformity was detected within the *P. strigosa* bacterial and archaeal microbiome across all tissue health types (Figure 8A).

Virus composition (RNA-Seq)

Across all samples, 107,696,252 raw and 61,629,374 normalized non-coral/non-Symbiodiniaceae reads remained after BBSplit and BBNorm. From the 946,025 rnaviralSPAdes-assembled putative viral scaffolds, MVP identified 728,070 putative viruses (77 to 20,239 bp; mean = 488.32 bp) before clustering/filtering, 12,608 vOTUs (97 to 15,068 bp; mean = 804.61 bp) after filtering, and 49 vOTUs (277 to 5,580 bp; mean = 2,943.69 bp) after clustering and filtering (Supplemental File 1: Table 6). Of these 49 vOTUs, two were scored as high quality by CheckV: vOTU20 (Order Ortervirales; Family Retroviridae) and vOTU27 (undescribed taxonomy). vOTU20 has two open reading frames (ORFs), one annotated as an integrase zinc binding domain and the other unannotated functionally, and vOTU27 has two unannotated ORFs (Supplemental File 2: Figure 8). These 49 vOTUs comprised both DNA and RNA viruses across Duplodnaviria (dsDNA genome), Varidnaviria (dsDNA genome), and Riboviria (RNA genome) Realms (Supplemental File 1: Table 6 and Supplemental File 2: Figure 9). vOTU alpha and beta diversity did not differ between tissue health states based on a Kruskal-Wallis rank sum test ($\chi^2 = 1.82$, df = 2, $p = 0.4025$) and a PERMANOVA test (df = 2, SumOfSqs = 0.07133, $R^2 = 0.14223$, $F = 0.9949$, $p = 0.382$), respectively (Figure 8B). DESeq2 tests of vOTU differential abundance across health state identified two vOTUs as significantly more abundant in HH tissues compared to both HD and DD tissues: vOTU11 and vOTU24 (both are bacteriophages in the Class Caudoviricetes). These were the only significant patterns of differential abundance; no vOTUs were significantly enriched in either HD or DD tissues compared to other health states.

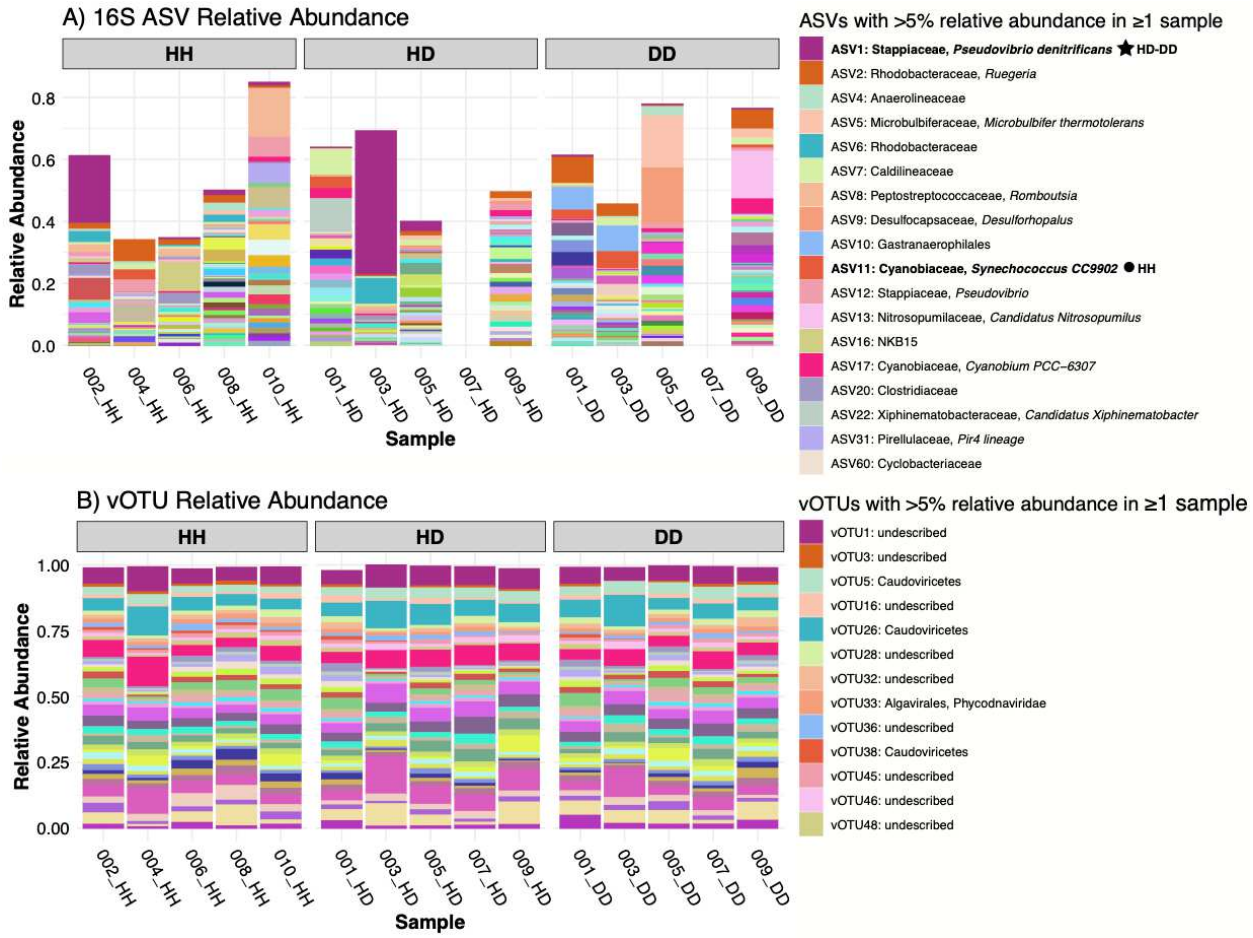


Figure 8: Relative abundance of bacterial/archaeal amplicon sequence variants (ASVs) representing > 0.01 of the community in at least one sample from 16S sequencing (A) and viral operational taxonomic units (vOTUs) representing > 0.01 of the community in at least one sample from RNA-Seq data (B). The ASV and vOTU taxonomy lists are abbreviated for practical purposes, showing taxa with relative abundance > 0.05 in at least one sample; the full list of ASVs and vOTUs plotted can be found in Supplemental File 2: Figures 19 and 20, respectively. Differential abundance testing found ASV1 to be significantly depleted between HD and DD tissue states (★). Consistent ASVs were defined as present in > 80 % of samples within a tissue state, and greater than 0.0005 relative abundance; only ASV11 was identified, and in HH (●). Health states are abbreviated for: HH: apparently healthy tissue on an apparently healthy coral; HD: apparently healthy tissue on a diseased coral; DD: lesion-adjacent tissue. ASV taxonomy is shown as the Family followed by the genus and species (if known), or the last known rank if Family is undescribed. vOTU taxonomy is shown as the Order followed by the Family, or the last known rank if Family is undescribed.

Microbial integration

No alpha or beta diversity indices were significantly correlated between bacteria/archaea, Symbiodiniaceae, and viruses. There were no significant correlations between ASV, ITS-2 type

profile, or vOTU Shannon diversity indices (Supplemental File 1: Table 7) in global, HH-only, HD-only, or DD-only comparisons based on Spearman correlations (Supplemental File 1: Table 8; Supplemental File 2: Figure 10). PCoA ordination results are summarized in Supplemental File 1: Table 9. Similarly, there were no significant correlations between ASV, ITS-2 type profile, or vOTU Bray-Curtis dissimilarity matrices based on Mantel tests (Supplemental File 1: Table 10) and within-dataset PCoA ordinations could not be overlaid with statistical significance based on Procrustes analyses (Supplemental File 1: Table 11 and Supplemental File 2: Figure 11). No associations between microbial taxa from the three microbial datasets were statistically significant. For pairwise comparisons of proportional associations between microbial taxa (Supplemental File 2: Figure 12), the FDR estimates were high (> 0.67) for all tested rho cutoffs (Supplemental File 1: Table 12). Thus, proportional associations could not be assessed due to low statistical power. The global network had 30 nodes, 24 edges, and 7 Louvain communities (Supplemental File 2: Figure 13), whereas the HH-specific network had 0 nodes, edges, and communities, and the HD- and DD-specific networks each had 2 nodes, 1 edge (HD: vOTU3-vOTU32; DD: vOTU29-vOTU30), and 1 community. The global network had edge density = 0.05517241, modularity = 0.7838542, and transitivity = 0 (Supplemental File 1: Table 13). In all networks, all nodes were vOTUs, and all associations were positive except the vOTU29-vOTU30 node in the DD-only network (Supplemental File 1: Table 14). No edges were shared between networks.

Microscopy and metatranscriptomics integration

In *P. strigosa,* a total of 47 WGCNA modules were identified in correlation with the disease phenotypes from histopathology and TEM analyses. Of the modules identified, 17 top modules were used for GO enrichment analysis for genes correlated to average vacuole area, average Symbiodiniaceae area, proportion of icosahedral virus-like particles, proportion of multi-membrane vesicles and proportion of cells with starch granules (Supplemental File 2: Figure 14). There were no top modules from coral host gene expression negatively associated with an increased proportion of multi-membrane vesicles in Symbiodinaceae cells in diseased coral tissue, as well as no top modules from coral host gene expression associated with the proportion of cells with starch granules.

In *Breviolum,* a total of 27 modules were identified in correlation to the disease phenotypes from histopathology and TEM analyses. Of the modules identified, 11 top modules were used for GO enrichment analysis or genes correlated to average vacuole area, average Symbiodiniaceae area, proportion of icosahedral virus-like particles, proportion of multi-membrane vesicles and proportion of cells with starch granules (Supplemental File 2: Figure 15).

Modules with a positive association correspond to an increase of genes when there are larger vacuoles and Symbiodiniaceae in healthy corals, high proportion of icosahedral virus-like particles, multi-membrane vesicles and starch granules in diseased corals (Table 2). Modules

with a negative association correspond to an increase in genes when there are smaller vacuoles and Symbiodiniaceae in diseased corals, low proportion of icosahedral virus-like particles, multi-membrane vesicles and starch granules in healthy corals (Table 2).

.

Three vOTUs were significantly differentially abundant across microscopy characteristics based on integrative DESeq2 analyses. vOTU25 (Realm Varidnaviria, Phylum Nucleocytoviricota, Class Megaviricetes, Order Pimascovirales, Family Ascoviridae) was significantly enriched in samples with larger Symbiodiniaceae and vacuole areas (as measured in the histopathology analysis), whereas vOTU21 (Realm Varidnaviria, Phylum Preplasmiviricota, Class Polintoviricetes, Order Orthopolintovirales, Family Adintoviridae) exhibited the opposite pattern and was enriched in samples with smaller Symbiodiniaceae and vacuole areas (Figure 4 M-N). vOTU11 (Realm Duplodnaviria, Phylum Uroviricota, Class Caudoviricetes) was significantly depleted in samples with a higher proportion of cells with spherical/icosahedral VLPs (based on TEM analyses). No vOTUs were significantly differentially abundant by proportion of cells with starch granules and MMVs.

Disease Phenotype	Top WGCNA Assocation & Modules			GO Enrichments
Average Vacuole Area	P.strigosa	Negative	White Darkmagenta Salmon Darkorange (744 transcripts)	Serine-type endopeptidase activity, SNARE interactions in vesicular transport (FDR = 2.50×10^{-3}), Intra-Golgi traffic (FDR = 6.60×10^{-3}), Protein-macromolecule adaptor activity (FDR = 2.62×10^{-2}), SNAP receptor activity (FDR = 3.35×10^{-2}), SNARE binding (FDR = 3.35×10^{-2}), Protein binding (FDR = 4.62×10^{-2}), Signaling by Receptor Tyrosine Kinases (FDR = 9.98×10^{-5})
		Positive	Purple (270 transcripts)	Transcription-Coupled Nucleotide Excision Repair (TC-NER) (FDR = 3.79×10^{-5}), RNA Polymerase II Transcription Initiation (FDR = 6.41×10^{-5}), Gap-filling DNA repair synthesis and ligation in TC-NER (FDR = 1.80×10^{-4}), RNA Polymerase II Transcription (FDR = 5.80×10^{-4}), DNA Repair (FDR = 7.10×10^{-4})
	Breviolum	Negative	Salmon Pink Yellow Darkorange Turquoise (1948 transcripts)	Serine-type endopeptidase activity, SNARE interactions in vesicular transport (FDR = 2.50×10^{-3}), Intra-Golgi traffic (FDR = 6.60×10^{-3}), Protein-macromolecule adaptor activity (FDR = 2.62×10^{-2}), SNAP receptor activity (FDR = 3.35×10^{-2}), SNARE binding (FDR = 3.35×10^{-2}), Protein binding (FDR = 4.62×10^{-2}), Signaling by Receptor Tyrosine Kinases (FDR = 9.98×10^{-5})
		Positive	Lightyellow Green Orange Red (593 transcripts)	Transcription-Coupled Nucleotide Excision Repair (TC-NER) (FDR = 3.79×10^{-5}), RNA Polymerase II Transcription Initiation (FDR = 6.41×10^{-5}), Gap-filling DNA repair synthesis and ligation in TC-NER (FDR = 1.80×10^{-4}), RNA Polymerase II Transcription (FDR = 5.80×10^{-4}), DNA Repair (FDR = 7.10×10^{-4})
Average Symbiodiniaceae Area	P.strigosa	Negative	White Magenta Salmon Lightgreen (744 transcripts)	Membrane Trafficking (FDR = 5.81×10^{-7}), Vesicle-mediated transport (FDR = 7.74×10^{-7}), Golgi-to-ER retrograde transport (FDR = 1.30×10^{-4}), SNARE interactions in vesicular transport (FDR = 1.20×10^{-3}), SNARE interactions in vesicular transport (FDR = 1.20×10^{-3}), Signaling by Receptor Tyrosine Kinases (FDR = 3.98×10^{-2}), Endocytosis (FDR = 4.89×10^{-2}), Cytokine Signaling in Immune system (FDR = 4.93×10^{-2})
		Positive	Yellowgreen (91 transcripts)	Apoptosis - multiple species (FDR = 1.59×10^{-2}), N-Glycan biosynthesis (FDR = 1.60×10^{-2}), Various types of N-glycan biosynthesis (FDR = 2.07×10^{-2})
	Breviolum	Negative	Salmon Darkgreen (379 transcripts)	Organic substance metabolic process (FDR = 1.23×10^{-45}), Macromolecule metabolic process (FDR = 1.78×10^{-35}), TP53 Regulates Metabolic Genes (FDR = 6.35×10^{-19}), Proteolysis (FDR = 1.92×10^{-14}), Cellular responses to stress (FDR = 3.25×10^{-10}), Phospholipid metabolism (FDR = 1.73×10^{-8}), Metabolic pathways (FDR = 3.67×10^{-8}), Glycerolipid biosynthetic process (FDR = 5.69×10^{-8}), Endocytosis (FDR = 9.25×10^{-8})
		Positive	Lightyellow Green Orange Red (249 transcripts)	Catalytic activity (FDR = 3.67×10^{-35}), Proteasome (FDR = 1.78×10^{-28}), APC/C-mediated degradation of cell cycle proteins (FDR = 5.38×10^{-27}), Antigen processing-Cross presentation (FDR = 8.88×10^{-27}), KEAP1-NFE2L2 pathway (FDR = 3.00×10^{-24}), Metabolic pathways (FDR = 3.09×10^{-15}), Fatty acid metabolism (FDR = 4.92×10^{-13}), Glutamate-ammonia ligase activity (FDR = 2.94×10^{-9})
Proportion of Icosahedral Virus-like Particles	P.strigosa	Negative	Darkorange2 Orange (313 transcripts)	mRNA processing (FDR = 7.00×10^{-3}), RNA binding (FDR = 1.20×10^{-2}), Spliceosomal activity (FDR = 2.20×10^{-3})
		Positive	Saddlebrown (109 transcripts)	rRNA processing (FDR = 1.93×10^{-12}), Ribosome biogenesis (FDR = 1.93×10^{-12}), RNA metabolic process (FDR = 2.01×10^{-8})
	Breviolum	Negative	Lightyellow Green (1326 transcripts)	Biosynthetic process (FDR = 5.89×10^{-47}), Protein metabolic process (FDR = 4.03×10^{-53}), Protein processing in endoplasmic reticulum (FDR = 1.27×10^{-6}), Oxidative phosphorylation (FDR = 8.73×10^{-6}), Metabolism of proteins (FDR = 1.47×10^{-39})
		Positive	Darkorange Yellow Pink (1844 transcripts)	Ion transport (FDR = 5.92×10^{-53}), Response to stress (FDR = 8.05×10^{-9}), Plant-pathogen interaction (FDR = 7.48×10^{-25}), Cell communication (FDR = 6.38×10^{-30}), Cellular component organization (FDR = 1.12×10^{-34}), Ion binding (FDR = 3.10×10^{-174}), Endocytosis (FDR = 1.10×10^{-3}), Innate immune system (FDR = 4.32×10^{-3})
Proportion of Multi-Membrane Vesicles	P.strigosa	Positive	Paleturquoise White Steelblue Plum1 (416 transcripts)	Regulation of transcription by RNA polymerase II (FDR = 3.73×10^{-2}), Serine-type endopeptidase activity (FDR = 3.20×10^{-3}), Transcription cis-regulatory region binding (FDR = 8.50×10^{-3}), P53 Regulates Transcription of Cell Cycle Genes (FDR = 3.08×10^{-2})
	Breviolum	Negative	Green (1159 transcripts)	Catalytic activity (FDR = 2.36×10^{-74}), Ubiquitin mediated proteolysis (FDR = 2.88×10^{-5}), Metabolism of proteins (FDR = 1.09×10^{-39}), Eukaryotic Translation Initiation (FDR = 1.23×10^{-31})
		Positive	Lightcyan Darkturquoise Pink Midnightblue (1052 transcripts)	Innate immune system (FDR = 4.60×10^{-4}), Arginine and proline metabolism (FDR = 4.34×10^{-9}), Biosynthesis of amino acids (FDR = 8.73×10^{-5}), Ether lipid metabolism (FDR = 1.80×10^{-4}), Metabolism (FDR = 2.22×10^{-16})
Proportion of Cells with Starch Granules	Breviolum	Negative	Darkgreen (138 transcripts)	Catalytic activity (FDR = 1.31×10^{-12}), Endocytosis (FDR = 8.97×10^{-9}), Macromolecule localization (FDR = 2.63×10^{-14}), Metabolic process (FDR = 1.72×10^{-17}), Nuclear Envelope Breakdown (FDR = 9.61×10^{-11}), Organic substance metabolic process (FDR = 8.78×10^{-19}), Phosphatidylinositol signaling system (FDR = 1.57×10^{-8}) and SUMOylation of DNA replication proteins (FDR = 3.34×10^{-10})
		Positive	Orange (81 transcripts)	Transport of vitamins, nucleosides, and related molecules (FDR = 4.03×10^{-6}), Metabolic pathways (FDR = 5.11×10^{-5}), Lipid metabolic process (FDR = 1.70×10^{-4}), Metabolism of carbohydrates (FDR = 9.10×10^{-4}), Fatty acid metabolism (FDR = 3.00×10^{-3}), The phototransduction cascade (FDR = 1.81×10^{-2}), Inactivation, recovery and regulation of the phototransduction cascade (FDR = 1.81×10^{-2})

447

Table 2: Summary of top WGCNA modules and GO Enrichment Analysis of *P. strigosa* and *Breviolum* associated modules to disease phenotypes from histology and TEM analyses. False discovery rate (FDR) for each GO enrichment term from String DB.

Discussion

Our integrative analyses suggest the unidentified coral disease outbreak at FGB in August 2022 is most consistent with WP. Here, we present the first characterizations of WP in *P. strigosa* across multiple biological data types. Our findings suggest that the disease manifests as a nutrient limitation-driven dysbiosis that may ultimately contribute to the tissue loss observed in diseased colonies. These results provide an important baseline characterization of WP in *P.strigosa* and offer an integrative framework to compare with other coral tissue loss diseases such as SCTLD.

Evidence of coral-Symbiodiniaceae dysbiosis and nutrient deficiency in diseased corals

Our data suggests that WP in *P. strigosa* induces coral–Symbiodiniaceae dysbiosis. In the coral host, the dysbiosis is characterized by immune activation, increased protein degradation pathways and shrinking of the vacuole that houses Symbiodiniaceae. These host-level changes likely restrict nutrient exchange, contributing to Symbiodiniaceae shrinkage and impaired metabolic function. Together, these findings suggest that WP disrupts the coral–Symbiodiniaceae symbiosis, resulting in coordinated stress responses that may ultimately contribute to tissue loss and mortality.

Host gene expression networks suggest that the coral host is mounting an active immune response to the disease. Differential gene expression shows upregulation in genes involved in protein degradation that may be counteracting and fighting gastrodermal necrosis. *Calnexin*, a calcium-binding ER protein that targets misfolded proteins for degradation, may indicate that the tissue is responding to the disease stress by targeting damaged or ineffective proteins. This response has previously been observed in cnidarians under stress conditions [34]. *Proteasome subunit alpha type-1*, a component of the 20S core proteasome complex, was also upregulated, suggesting increased degradation of damaged and/or misfolded proteins in response to disease. Additional evidence of targeting degraded proteins is demonstrated by an upregulation of *U-actitoxin-Avd3n*, a serine protease inhibitor associated with protective anti-inflammatory responses and regulation proteolytic activity [35]. The upregulation of these genes in diseased colonies suggests that the coral host is actively responding to disease stress and attempting to preserve surrounding healthy tissue.

Linking the shrinking of size of both the Symbiodiniaceae-hosting vacuole and Symbiodiniaceae cells with gene expression patterns revealed that diseased colonies are enriched in receptor tyrosine kinases (RTKs) and cytokine signalling. RTK signalling is consistent with an active immune response, as receptor tyrosine kinases are known to be involved in inflammatory

signalling cascades including MAPK and cytokine production [36,37]. RTKs have been identified in response to coral disease, consistent with a role in coordinating the host immune response [38]. Because cytokines function as small protein messengers and immune effectors that mediate immune response, these enrichment patterns connect the host immune activation and the breakdown of symbiosis [39]. This active immune response may divert energy resources to defense rather than maintenance of symbiosis, causing host-regulated nutrient restriction [40]. As a result, the observed shrinkage of the Symbiodiniaceae cells may represent a stress response to reduced nutrient availability from the host.

Nutrient restriction to Symbiodiniaceae is evident in additional ways beyond shrinkage. Electron micrographs revealed abnormalities in the Symbiodiniaceae cells, such as increased proportion of cells with starch granules in diseased tissues, enrichments for pathways involved in the phototransduction cascade, lipid, carbohydrate and fatty acid metabolism, as well as changes in transport of nutrients such as vitamins. These results outline a nutrient imbalance in the Symbiodiniaceae cells, which has been seen to manifest in an accumulation of starch granules [41,42] as well as prior work showing Symbiodiniaceae altering transport and metabolic pathways under nutrient restriction and stress [43–45]. This provides further evidence that the starch granules may be a method of energy storage during host-restricted nutrient supply in response to the disease. The integration of histopathological, TEM, and transcriptomic evidence suggests that the Symbiodiniaceae in diseased tissues enter an energetically conservative and storage-oriented state as a consequence of the host's resource allocation in response to the disease.

Other observed abnormalities in Symbiodiniaceae cells suggest further evidence of metabolic imbalances. Electron micrographs of some Symbiodiniaceae cells contained highly organized structures of concentric rings, hereafter multi-membrane vesicles (MMVs, Figure 5 A-B). These MMVs were present in higher proportions of Symbiodiniaceae cells sampled from lesion-adjacent tissues compared to those sampled from apparently healthy tissues. MMVs could reflect a stress response of Symbiodiniaceae cells, as they could be lamellar bodies formed during lipid storage/secretion, which is reflected in the gene enrichments associated with higher proportions of MMVs in DD tissue [46,47]. Another possibility is that the MMVs are starch granules themselves if Symbiodiniaceae shift from floridean starch production to those reminiscent of starch granules in higher plants, characterized by alternating amorphous and semi-crystalline layers [48], though further alternative interpretations of the MMVs are possible. We observed a higher proportion of cells with starch granules in Symbiodiniaceae sampled from diseased corals compared to those sampled from apparently healthy corals. Starch storage has been proposed as a stress response in Symbiodiniaceae isolated from soft corals [42]. Thus, it is possible that the MMVs present in Symbiodiniaceae adjacent to disease lesions reflect starch storage as Symbiodiniaceae cells become stressed.

Metabolic changes in WP-affected coral holobionts may be mediated by viral infections. Shrunken Symbiodiniaceae cells and vacuoles housing them were associated with the enrichment of a putative DNA viral lineage in the Order Orthopolintovirales. This viral Order contains dsDNA viruses in the Class Polintiviricetes, which is comprised of polintons and polinton-like viruses that have been identified as integrated elements in stony coral genomes [49] and have been shown to infect protists [50,51]. While we cannot distinguish a eukaryotic host within the coral holobiont for this virus, it may contribute to histopathological WP phenotypes. For example, viral infection or the integration of Orthopolintovirales-like elements may carry genes that alter host cell metabolism or size without lysing host cells, potentially contributing to altered Symbiodiniaceae/vacuole areas [51].

***Integrative characterization of white plague in* P. strigosa**

Based on our observations of this disease, we hypothesize WP in *P. strigosa* presents as coral-Symbiodiniaceae dysbiosis resulting from a breakdown of host-symbiont nutrient transfer that alters Symbiodiniaceae metabolism. Our findings suggest WP is characterized by a feedback loop wherein the coral mounts an initial immune response that limits nutrients to its associated Symbiodiniaceae resulting in coral-Symbiodiniaceae dysbiosis characterized by altered expression of metabolism genes, shrinkage of Symbiodiniaceae cells and the vacuoles housing them, and the accumulation of starch granules and/or lamellar bodies, which is potentially mediated by DNA viruses.

A clear etiologic role for microorganisms in the WP-like disease was not detectable based on our analyses of archaeal, bacterial, Symbiodiniaceae, and viral communities (likely due to limited statistical power). Amplicon sequencing of the 16S rRNA gene revealed high variability and no uniformity within *P. strigosa* bacterial/archaeal communities across all tissue types. However, such variation has been documented in healthy *P. strigosa* tissues [52], and the dysbiotic state from these *P. strigosa* corals is notable because dysbiosis thresholds may increase WP susceptibility [15]. One consistency in the dataset is *Synechococcus*, a common coral cyanobacteria [53,54] associated with the healthy corals, potentially confirming the control corals as healthy and suggesting that WP results in the loss of these bacteria.

The dominant Symbiodiniaceae lineage in these *P. strigosa* corals was not affected by this WP-like disease; however, this is unsurprising given the depth of the FGB, historic specificity in Symbiodiniaceae associations of FGB *P. strigosa* [55], and the fact that all sampled colonies were dominated by a single Symbiodiniaceae lineage [56]. Electron micrographs revealed some evidence of putative viral infection of Symbiodiniaceae cells from diseased corals, namely putative +ssRNA viral replication bodies (an alternative interpretation of the MMVs; [57,58] and spherical/icosahedral VLPs, but there were no metatranscriptomic signatures of viral infection associated with DD tissues (only histopathological characteristics of DD tissues). We hypothesize that viruses may interface with WP in *P. strigosa* or FGB corals differently than in

other coral species or biogeographic regions. Eukaryotic circular Rep-encoding single-stranded DNA viruses and their associated satellites (SCSDVs) have been associated with WP-affected tissues in *Montastraea cavernosa* in the U.S. Virgin Islands [14]. In Brazil, WP-affected *Mussismilia braziliensis* contained higher abundances of primarily cyanobacteria-infecting bacteriophages (Families Myoviridae and Siphoviridae) than apparently healthy conspecifics, which tracked the proliferation of opportunistic cyanobacteria [13]. Furthermore, WP does not appear to consistently affect multi-Domain and viral interactions in the *P. strigosa* holobiont. Alpha and beta diversity metrics were not correlated across communities of archaea/bacteria, Symbiodiniaceae, and viruses in global or health-state-specific analyses. This could suggest these microbial communities are shaped by other factors, such as environmental covariates [59–61].

The lack of identification of an etiological agent or clear significant correlations between these communities is likely due to low statistical power stemming from our low sample size. Future studies with expanded sample sizes will be better able to discern how WP affects microbial communities. However, we were able to generate specific hypotheses related to host and Symbiodiniaceae function based on other data types. As the first study to use these methods to study a WP-like disease in *P. strigosa*, our hypotheses should guide future research efforts that further investigate signatures of WP across an expanded sample size.

Identified differences between WP and SCTLD

Through our integrative approach, we demonstrate that the acute tissue loss disease outbreak at FGB is consistent with WP and differs substantially from SCTLD across cellular, microbial, viral, and gene expression scales. While both diseases result in acute tissue loss and disruption of coral–Symbiodiniaceae symbiosis, the mechanisms and signatures appear to be different. SCTLD is characterized by swollen Symbiodiniaceae and Symbiodiniaceae-housing vacuoles [10], symbiophagy [10], depletion of starch granules [12], filamentous VLPs in Symbiodiniaceae cells [12], widespread viral opportunism characterized by heightened viral production and/or novel infection across various DNA and RNA viral lineages (including putative Symbiodiniaceae-infecting viruses in the classes Megaviricetes and Duplopiviricetes) [8,23,62,63]. In contrast, we characterize WP as exhibiting shrunken Symbiodiniaceae and Symbiodiniaceae-housing vacuoles, accumulation of starch granules in Symbiodiniaceae cells, no evidence of symbiophagy, and associations with a different class of DNA, but not RNA, viruses (Polintoviricetes). As for microbial differences, there was high variability and no uniformity in archaeal/bacterial communities, while SCTLD shows more consistent communities across tissue types in *P. strigosa* [25]. Furthermore, our results exhibit a host-mediated nutrient limitation to Symbiodiniaceae, representing a different cause of dysbiosis than SCTLD. Together, these findings suggest that although both diseases disrupt coral–Symbiodiniaceae symbiosis, they likely do so through distinct mechanisms and host–symbiont interactions.

Conclusions

Based on our holistic characterization of the disease, disease monitoring, and coral recovery from 2023 to 2024, we characterize the 2022 FGB coral disease outbreak as white plague. We further model an integrative framework that can be used to guide management/intervention actions and characterize future coral disease outbreaks across gene, sub-cellular, and cellular levels of diverse members of the coral holobiont. Integrative analyses drastically expanded our ability to understand and characterize WP, particularly through microscopy and metatranscriptomic integrations. While several of our metrics showed low or no different expression/abundance across tissue health states either due to low replication or lack of robustness in the biological signal, many did show correlative patterns which helped contextualize the data. Specifically, integrating archaeal/bacterial and Symbiodiniaceae amplicon sequencing with host and viral metatranscriptomics merits further use for robust assessments of microbial networks/interactions within the coral holobiont.

Methods

Sample collection

Following the disease outbreak, fifteen *Pseudodiploria strigosa* samples were collected from Flower Garden Banks National Marine Sanctuary at West Flower Garden Bank (Buoy 2: 27°52.526 N, −93°48.836 W; Buoy 5: 27°52.519 N, −93°48.889 W) and East Flower Garden Bank (Buoy 2: 27°54.516 N, −93°35.831 W) (Figure 1). Samples were collected via SCUBA at 18–24 m depth using a hammer and chisel. Corals (N = 10 colonies) were sampled in situ as paired diseased and apparently healthy tissues. From each diseased colony, two samples were collected: one adjacent to the lesion (DD; n = 5) and one from apparently healthy tissue on the same colony (HD; n = 5). An additional sample was collected from a neighboring apparently healthy colony (HH; n = 5). Each sample was divided into three fragments and fixed accordingly for histopathology, transmission electron microscopy (TEM), and DNA/RNA sequencing (Figure 2). See Methods S01 for further details.

Histopathology imaging and analysis

Samples were decalcified in 1% HCl–EDTA and stored in 70% ethanol until processing. Tissues were serially dehydrated and cleared with xylenes using a Leica ASP6025 tissue processor, embedded in paraffin (Leica EG1150H), and sectioned at 5 µm thickness on a Leica RM2125RTS microtome. For each sample, five serial sections were prepared approximately 500 µm apart. Sections were stained with hematoxylin and eosin (Leica ST5020), imaged using an Olympus BX41 microscope with an SC180 camera, and analyzed in ImageJ. A quantitative histopathological diagnostic framework following Rossin et al. (2026; [11]) was applied to quantify vacuolization, exocytosis, gastrodermal separation, degraded Symbiodiniaceae, and Symbiodiniaceae and vacuole areas. Differences among health states were assessed using one-way analysis of variance (ANOVA) and Tukey post-hoc tests. See Supplemental File 3 for further details.

Transmission electron microscopy (TEM) imaging and analysis

Coral fragments ~3 mm^2 long (fixed in 750 µL of 2% PFA in 3X PBS) were decalcified in 1000 µL of 1.5% ascorbic acid for 7-14 days, replacing the ascorbic acid solution daily until the entire skeleton was dissolved. The decalcified samples were fixed in Karnovsky's fixative for at least 24 hours before being processed according to [17]. Electron micrographs were imaged using a 120 kV JEOL JEM-1400Flash Transmission Electron Microscope equipped with a high-contrast pole piece and a 15 megapixel AMT NanoSprint15 sCMOS camera. Electron micrographs showed 438 total Symbiodiniaceae cells: 123 from HH tissue (20-30 cells per sample), 142 from HD tissue (23-38 cells per sample), and 173 from DD tissue (27-46 cells per sample). Excluding 16 cells considered too degraded for downstream analysis (Supplemental File 2: Figure 16), 119 cells were analyzed from HH tissues, 136 from HD tissues, and 172 from DD tissues, for a total of 427 analyzed Symbiodiniaceae cells. All electron micrographs are available on BCO-DMO. Each cell was scored for the presence/absence of degradation characteristics, abnormalities, and putative viral characteristics. A cell was considered degraded if it contained ≥2 of the following: (i) indistinct organelles (< 2 identifiable organelles), (ii) an abnormal cell membrane (oblong or discontinuous), (iii) indistinct thylakoid membranes (blurred together or unevenly spaced), and (iv) large cavities. Other features/abnormalities included the absence of the pyrenoid body and starch granules. Putative viral characteristics included filamentous virus-like particles (VLPs), masses of filamentous VLPs, spherical/icosahedral VLPs, crystalline arrays of spherical/icosahedral VLPs, crystal structures, viroplasms (both whorled and non-whorled), and multi-membrane vesicles (MMVs). ImageJ (v1.54g) was used to measure the diameters of spherical/icosahedral VLPs and MMVs. Representative images of all features identified can be found in Supplemental File 2: Figure 17. All statistical analyses were performed in RStudio (v2023.06.2+561). Binomial logistic regressions and post-hoc pairwise comparisons of estimated marginal means were used to identify associations between health state and viral and/or degradation characteristics/abnormalities. See Supplemental File 3 for further details.

Nucleic acid extraction and sequencing

From each of the fifteen *Pseudodiploria strigosa* samples, a pea-sized subset was removed with sterilized bonecutters before airbrushing the remaining tissue with a PBS solution. The resultant slurry was airbrushed at maximum speed at 4°C for 40 minutes. DNA was extracted from ~0.040 g of the pellet with the Qiagen DNeasy PowerBioFilm Kit (Qiagen, Inc., Germantown, MD) and split into two aliquots. The DNA from one aliquot was used as the template for sequencing of Symbiodiniaceae internal transcribed spacer-2 (ITS-2) rDNA using the Sym_VAR primer set [64], and libraries were prepared and sequenced with 300 bp, paired-end sequencing on an Illumina MiSeq platform at Oregon State University's Center for Quantitative Life Sciences (OSU CQLS, Corvallis, OR, USA). The DNA from the second aliquot was used as the template for sequencing of the V4 region of the small subunit rRNA gene of bacteria/archaea using primers 515Y and 806RB [65,66], and sequencing was performed with 250 bp, paired-end

sequencing on an Illumina MiSeq platform at the University of Illinois at Urbana-Champaign [67]. For analysis of 16S sequences, two samples (HD and DD tissues from coral 007) were excluded due to a mislabeling error during laboratory processing. See Supplemental File 3 for further details.

Total RNA was extracted from the pea-sized subsets using the Invitrogen RNAqueous Kit (Invitrogen Corporation, Carlsbad, CA, AM1914) with Ambion DNase I (Thermo Fisher Scientific, Austin, TX, AM2222) to remove genomic contamination. For DD samples, tissue was collected ~1 – 2 cm from the lesion margin. Total RNA aliquots were sent to Novogene Co., LTD for library preparation and 150 bp, paired-end sequencing with poly-A tail enrichment on the Illumina Novaseq 6000 platform. See Supplemental File 3 for further details.

Analysis of Symbiodiniaceae composition

Symbiodiniaceae ITS-2 rDNA sequences were run against the remote SymPortal database (SymPortal.org; [68]) to identify Symbiodiniaceae taxonomy as ITS-2 type profiles. The SymPortal output was imported into RStudio (v2023.06.2+561) with the phyloseq package (v1.48.0; [69]). Based on a rarefaction curve (Supplemental File 2: Figure 18), all samples had sufficient sequencing depth to be included in downstream analyses. Between-genus ITS-2 copy number variation was accounted for according to previously described methods [17]. Per-sample ITS-2 type profile absolute abundances were converted to relative abundances for ggplot2 (v3.5.2; [70]-generated bar plots and PERMANOVA tests to assess whether Symbiodiniaceae ITS-2 type profile composition varied between tissue health states. See Supplemental File 3 for further details.

Analysis of bacteria and archaea composition

Bacteria/archaea 16S rRNA gene amplicon sequencing data were processed in RStudio (v.4.4.0) using the DADA2 pipeline (dada2v.1.16; [71]). Demultiplexed fastq files were quality filtered, merged, and used to infer amplicon sequence variants (ASVs). Taxonomy was assigned with the Silva reference database (v.138.1; [72]), and the resulting ASV count, taxonomy, and metadata tables were imported into phyloseq (v.1.48.0) for downstream analyses. Variation in beta diversity by health state was visualized with a principal component analysis using Aitchison distance [73] and was statistically assessed using PERMANOVA with adonis2 from the vegan package (v.2.6.0; [74]). Differences in similarity by health state were assessed with average similarity percentage (SIMPER), and differential relative abundance of ASVs across health states was tested with the corncob package (v.0.4.1). Taxa present in >80% of samples within a tissue state and with >0.05% relative abundance were used to determine whether the *P. strigosa* samples had a core microbiome. See Supplemental File 3 for further details.

De novo *transcriptome assembly, annotation and differential gene expression analysis*

Raw Illumina NovaSeq reads from *Pseudodiploria strigosa* were quality filtered and trimmed using FastP (v0.23). The six samples with the highest read quality (Q30 > 90%) were used to generate a *de novo* metatranscriptome assembly with Trinity (v2.15.1) on the University of Texas – Arlington's High Performance Computing Cluster. Coral host transcripts were identified by extracting longest isoforms and performing BLASTn (v2.15.0) searches against a curated coral reference database.

To isolate coral and Symbiodiniaceae reads, BBsplit (v38.79) was used to map reads to the *P. strigosa* transcriptome and Symbiodiniaceae reference transcriptomes from *Symbiodinium* [75], *Breviolum* [76], *Cladocopium* [77], and *Durusdinium* [43]. Unmapped reads were retained for downstream viral metatranscriptomic analyses. The dominant Symbiodiniaceae genus was identified as *Breviolum* based on transcript abundance. *P. strigosa* and Symbiodiniaceae reads were retained as paired-end files for quantification.

Transcript abundance was quantified using Salmon (v1.4.0) with quasi-mapping against reference transcriptomes for *P. strigosa* and *Breviolum*. Gene-level count matrices were generated in R (v4.4.1) using tximport (v1.30.0). Differential gene expression analyses were performed using DESeq2 (v1.42.0) with the design ~ *Site* + *Health_State*. Lowly expressed genes (mean count < 10) were removed, and data were rlog-transformed for visualization. Differentially expressed genes (DEGs) were identified using thresholds of $|\log_2 \text{fold change}| \geq 1$ and adjusted p-value ≤ 0.05 across health state contrasts (HH vs HD, HH vs DD, HD vs DD). Principal component analysis (PCAtools v2.14.0) was used to assess sample clustering and identify outliers. DEGs were annotated against the UniProt database. See Supplemental File 3 for further details.

Analysis of viral composition

The BBsplit-generated unmapped reads were normalized with bbnorm.sh within BBMap (v39.09; [78]). *De novo* transcriptome assembly was performed with rnaviralSPAdes using the option --rnaviral in SPAdes (v4.1.0; kmers: 21, 33, 55, 77; [79]). MVP (v1.1.4; [80]) was used to annotate and map reads to the assembled scaffolds, which were clustered into viral operational taxonomic units (vOTUs) with CheckV (v1.0.1; [81]) based on the MIUVIG-recommended parameters of 95% average nucleotide identity and 85% alignment fraction [82]. The MVP-generated vOTU abundance tables (normalized to reads per kilobase per million reads: RPKM) were imported into RStudio (v2023.06.2+561) with the phyloseq package (v1.48.0; [83]). vOTU composition and diversity were visualized and/or analyzed with relative abundance bar plots, alpha/beta diversity analyses, and differential abundance tests. See Supplemental File 3 for further details.

Integration of microbial and viral communities

To perform integrative analyses of bacterial/archaeal (ASV), Symbiodiniaceae (ITS-2 type profile), and viral (vOTU) communities, raw counts were converted to relative abundances and

766 filtered taxa not present at ≥1% abundance in ≥1 sample. Spearman correlation and Mantel tests
767 were used to compare whether within-dataset alpha and beta diversity metrics were correlated
768 across datasets in both global and health-state-specific subsets of the data. Procrustes analyses
769 were used to test whether ordinations of Bray-Curtis dissimilarity matrices could be
770 superimposed.
771
772 Pairwise correlations and network analyses on a concatenated table of ASV, ITS-2 type profile,
773 and vOTU relative abundance in all samples and HH-, HD-, and DD-only samples were used to
774 assess the significance of putative interactions between microbial taxa. The propr package
775 (v5.1.8; [84]) was used to test whether individual taxa covaried across samples, wiith the
776 UpdateCutoffs() function used to calculate the false discovery rate (FDR). Co-occurrence
777 networks were created with the FlashWeave package (v0.19.2; [85]) in Julia (v1.10.2; [86]). A
778 tidygraph object from the network was created using the tbl_graph() function (directed =
779 FALSE) in the package tidygraph (v1.3.1; [87]) with Louvain community detection to identify
780 clusters of co-occurring microbial consortia or functional modules, and both node- and network-
781 level metrics were calculated. Due to low sample sizes, bootstrapping could not be performed to
782 statistically compare network statistics between networks. See Supplemental File 3 for further
783 details.
784
785 *Integration of microscopy and metatranscriptomic measures*
786 Regularized log expression (rlog) of *P. strigosa* and *Breviolum* were integrated with statistically
787 significant disease phenotypes as continuous variables from histopathology (average vacuole
788 area, average Symbiodiniaceae area) and TEM (proportion of spherical/icosahedral VLPs,
789 proportion of multi-membrane vesicles (MMV) and proportion of cells with starch granules)
790 using a Weighted Gene Co-Expression Network Analysis (WGCNA; v1.71; [88]). Top modules
791 were combined for each disease phenotype, and used in the STRING Database (v12.0;[89]). The
792 predicted protein sequence output file from Trandecoder was uploaded to STRING and used in
793 place of a proteome. WGCNA modules were separated by disease phenotype, into positive and
794 negative correlation gene sets. Gene sets were uploaded to STRING with the analysis criteria of
795 protein-protein interactions of high confidence (0.7) and an addition of protein interactions of no
796 more than 20 per gene set. Significant functional enrichments were identified and filtered for
797 enrichments in Biological Process, Molecular Function, KEGG Pathways and Reactome
798 Pathways. See Supplemental File 3 for further details.
799
800 Histopathology measurements and the proportion of cells with TEM characteristics were
801 integrated into vOTU differential abundance analyses as continuous variables in DESeq2. For
802 histopathology measurements, the average Symbiodiniaceae cell and vacuole areas had means >
803 5, so these variables were centered and scaled with the scale() function before running DESeq2.
804 The Log2 Fold Change ± standard error for vOTUs in these analyses were visualized using the
805 ggplot2 package (v3.5.2; [90]).

Abbreviations

ASV: Amplicon sequence variant
DD: Lesion-adjacent tissue on a diseased coral
FDR: False discovery rate
FGB: Flower Garden Banks National Marine Sanctuary
GO: Gene ontology
HH: Apparently healthy tissue on an apparently healthy coral
HD: Apparently healthy tissue on a diseased coral
ITS-2: Internal transcribed spacer-2
MMV: Multi-membrane vesicle
RTK: Receptor tyrosine kinase
SCTLD: Stony coral tissue loss disease
TEM: Transmission electron microscopy
VLP: Virus-like particle
vOTU: Viral operational taxonomic unit
WGCNA: Weighted Gene Co-Expression Network Analysis
WP: White plague

Declarations

Ethics approval and consent to participate
Not applicable

Consent for publication
Not applicable

Availability of data and materials
Electron micrographs and histology images are available in BCO-DMO submission XX. Raw ITS-2, RNA-Seq, and 16S rRNA gene sequences are available in the NCBI BioProject PRJNA1292163. Code for analysis is in XX GitHub repository.

Competing interests
The authors declare no competing interests.

Funding
This work was supported by NSF Rapid OCE-2530272, NSF EEID OCE-2109622, and Texas SeaGrant 2024GC2674.

Authors' contributions

CEK and HLS contributed equally to this article. AA, MB, DMH, LM, and AMSC conceived and designed the study. MAJ, MFN, and AMSC collected the samples. CEK, HLS, AMR, MK, GC, MC, LIH, and MDM processed the samples. CEK, HLS, AMR, MK, LIH, and MKO performed the statistical and computational analysis. CEK, HLS, AMR, MK, and LIH interpreted the data. CEK and HLS drafted the initial manuscript. All authors contributed to manuscript revision and approved the final version to be published.

Acknowledgements

We thank the FGB staff, Keisha Bahr, and Olivia Eisenbach for assistance with sample collection. We thank Kelsey Beavers, Alondra Franco, Daniela Gutierrez-Andrade, and Jada Jean for assistance with sample processing and/or analysis. Samples were collected under the permit FGBNMS-2019-001. The scientific results and conclusions, as well as any views or opinions expressed herein, are those of the author(s) and do not necessarily reflect the views of NOAA or the Department of Commerce. This publication does not constitute an endorsement of any commercial product or intend to be an opinion beyond scientific or other results obtained by the National Oceanic and Atmospheric Administration (NOAA).

References

1. Burke S, Pottier P, Lagisz M, Macartney EL, Ainsworth T, Drobniak SM, et al. The impact of rising temperatures on the prevalence of coral diseases and its predictability: A global meta-analysis. Ecol Lett. 2023;26(8):1466–81. doi:10.1111/ele.14266

2. Burge CA, Eakin CM, Friedman CS, Froelich B, Hershberger PK, Hofmann EE, et al. Climate Change Influences on Marine Infectious Diseases: Implications for Management and Society. Annu Rev Mar Sci. 2014 Jan 3;6(Volume 6, 2014):249–77. doi:10.1146/annurev-marine-010213-135029

3. Ritchie KB, Polson SW, Smith GW. Microbial disease causation in marine invertebrates: problems, practices, and future prospects. Hydrobiologia. 2001 Sep 1;460(1):131–9. doi:10.1023/A:1013181718805

4. Muller EM, van Woesik R. Caribbean coral diseases: primary transmission or secondary infection? Glob Change Biol. 2012;18(12):3529–35. doi:10.1111/gcb.12019

5. Landsberg JH, Kiryu Y, Peters EC, Wilson PW, Perry N, Waters Y, et al. Stony Coral Tissue Loss Disease in Florida Is Associated With Disruption of Host–Zooxanthellae Physiology. Front Mar Sci. 2020 Dec 16;7:576013. doi:10.3389/fmars.2020.576013

6. Pollock FJ, Morris PJ, Willis BL, Bourne DG. The Urgent Need for Robust Coral Disease Diagnostics. PLOS Pathog. 2011 Oct 20;7(10):e1002183. doi:10.1371/journal.ppat.1002183

7. Vega Thurber R, Mydlarz LD, Brandt M, Harvell D, Weil E, Raymundo L, et al. Deciphering Coral Disease Dynamics: Integrating Host, Microbiome, and the Changing Environment. Front Ecol Evol. 2020 Nov 30;8:575927. doi:10.3389/fevo.2020.575927

8. Vega Thurber RL, Silva D, Croquer A, Veglia AJ, Alvarez-Filip L, Zaneveld JR, et al. Coral Disease: Direct and Indirect Agents, Mechanisms of Disease, and Innovations for Increasing Resistance and Resilience. Annu Rev Mar Sci. 2025 Jan 16;17(Volume 17, 2025):227–55. doi:10.1146/annurev-marine-011123-102337

9. Cróquer A, Weil E, Rogers CS. Similarities and Differences Between Two Deadly Caribbean Coral Diseases: White Plague and Stony Coral Tissue Loss Disease. Front Mar Sci. 2021 Oct 18;8:709544. doi:10.3389/fmars.2021.709544

10. Beavers KM, Van Buren EW, Rossin AM, Emery MA, Veglia AJ, Karrick CE, et al. Stony coral tissue loss disease induces transcriptional signatures of in situ degradation of dysfunctional Symbiodiniaceae. Nat Commun. 2023 May 22;14(1):2915. doi:10.1038/s41467-023-38612-4

11. Rossin AM, Beavers KM, Karrick CE, Bloomberg J, Meiling S, Carpenter GE, et al. Runaway coral-algal dysbiosis may be responsible for rapid coral tissue loss. Sci Rep. 2026 Jan 27;16(1):6415. doi:10.1038/s41598-026-35666-4

12. Work TM, Weatherby TM, Landsberg JH, Kiryu Y, Cook SM, Peters EC. Viral-Like Particles Are Associated With Endosymbiont Pathology in Florida Corals Affected by Stony Coral Tissue Loss Disease. Front Mar Sci. 2021 Nov 5;8:750658. doi:10.3389/fmars.2021.750658

13. Silva-Lima AW, Froes AM, Garcia GD, Tonon LAC, Swings J, Cosenza CAN, et al. Mussismilia braziliensis White Plague Disease Is Characterized by an Affected Coral Immune System and Dysbiosis. Microb Ecol. 2021 Apr;81(3):795–806. doi:10.1007/s00248-020-01588-5

14. Soffer N, Brandt ME, Correa AMS, Smith TB, Thurber RV. Potential role of viruses in white plague coral disease. ISME J. 2014 Feb 1;8(2):271–83. doi:10.1038/ismej.2013.137

15. MacKnight NJ, Cobleigh K, Lasseigne D, Chaves-Fonnegra A, Gutting A, Dimos B, et al. Microbial dysbiosis reflects disease resistance in diverse coral species. Commun Biol. 2021 Jun 3;4(1):679. doi:10.1038/s42003-021-02163-5

16. MacKnight NJ, Dimos BA, Beavers KM, Muller EM, Brandt ME, Mydlarz LD. Disease resistance in coral is mediated by distinct adaptive and plastic gene expression profiles. Sci Adv. 2022 Sep 30;8(39):eabo6153. doi:10.1126/sciadv.abo6153

17. Howe-Kerr LI, Knochel AM, Meyer MD, Sims JA, Karrick CE, Grupstra CGB, et al. Filamentous virus-like particles are present in coral dinoflagellates across genera and ocean basins. ISME J. 2023 Dec 1;17(12):2389–402. doi:10.1038/s41396-023-01526-6

18. Dennison CE, Karp RF, Weiler BA, Goncalves A, del Campo J, Rosales SM, et al. The role of algal symbionts (genus Breviolum) in the susceptibility of corals to Stony Coral Tissue Loss Disease in South Florida | Florida Department of Environmental Protection [Internet]. 2021 [cited 2025 Dec 15]. Available from:

https://floridadep.gov/rcp/coral/documents/role-algal-symbionts-genus-breviolum-susceptibility-corals-stony-coral-tissue

19. Karp R, Dennison C, Kron K, Baker A. The use of algal symbiont cultures (Family Symbiodiniaceae) as model systems to study stony coral tissue loss disease: Use of fractionated disease isolates to help with pathogen identification | Florida Department of Environmental Protection [Internet]. 2023 [cited 2025 Dec 15]. Available from: https://floridadep.gov/rcp/coral-protection-restoration/documents/use-algal-symbiont-cultures-family-symbiodiniaceae-0

20. Klein AM, Sturm AB, Eckert RJ, Walker BK, Neely KL, Voss JD. Algal symbiont genera but not coral host genotypes correlate to stony coral tissue loss disease susceptibility among Orbicella faveolata colonies in South Florida. Front Mar Sci. 2024 Jan 25;11. doi:10.3389/fmars.2024.1287457

21. Papke E, Carreiro A, Dennison C, Deutsch JM, Isma LM, Meiling SS, et al. Stony coral tissue loss disease: a review of emergence, impacts, etiology, diagnostics, and intervention. Front Mar Sci. 2024 Jan 25;10:1321271. doi:10.3389/fmars.2023.1321271

22. Titus K, O'Connell L, Matthee K, Childress M. The Influence of Foureye Butterflyfish (Chaetodon capistratus) and Symbiodiniaceae on the Transmission of Stony Coral Tissue Loss Disease. Front Mar Sci. 2022 Mar 21;9:800423. doi:10.3389/fmars.2022.800423

23. Veglia AJ, Beavers KM, Van Buren EW, Meiling SS, Muller EM, Smith TB, et al. Holobiont-structured viromes and opportunistic viral infections in stony coral tissue loss disease-affected corals. in prep.

24. Kozachuk A, Jones NP, Williams GJ, Sharkey R, Klug K, Walker BK. Frequent coral disease interventions reduces tissue loss. Sci Rep. 2026 Mar 25. doi:10.1038/s41598-026-44748-2

25. Huntley N, Brandt ME, Becker CC, Miller CA, Meiling SS, Correa AMS, et al. Experimental transmission of Stony Coral Tissue Loss Disease results in differential microbial responses within coral mucus and tissue. ISME Commun. 2022 Dec;2(1):46. doi:10.1038/s43705-022-00126-3

26. Rosales SM, Huebner LK, Evans JS, Apprill A, Baker AC, Becker CC, et al. A meta-analysis of the stony coral tissue loss disease microbiome finds key bacteria in unaffected and lesion tissue in diseased colonies. ISME Commun. 2023 Dec 1;3(1):19. doi:10.1038/s43705-023-00220-0

27. Carpenter GE, Farmer BH, Craft HE, Apprill A, Brandt ME, Correa AMS, et al. Mesoscale Circulation and Coral Community Disturbance at Isolated Reefs. Glob Change Biol Commun. 2026;1(1):e70005. doi:10.1002/gcb4.70005

28. Johnston MA, Embesi JA, Eckert RJ, Nuttall MF, Hickerson EL, Schmahl GP. Persistence of coral assemblages at East and West Flower Garden Banks, Gulf of Mexico. Coral Reefs. 2016 Sep 1;35(3):821–6. doi:10.1007/s00338-016-1452-x

29. Borneman E. Pathologies affecting reef corals at the flower garden banks, northwestern Gulf of Mexico. Gulf Mex Sci. 2005.

30. Hickerson EL, Schmahl G, Robbart M, Precht WF, Caldow C. The state of coral reef ecosystems of the Flower Garden Banks, Stetson Bank, and other banks in the northwestern Gulf of Mexico. State Coral Reef Ecosyst U S Pac Free Assoc States. 2008;189–217.

31. Schmahl GP, Hickerson EL, Precht WF. Biology and ecology of coral reefs and coral communities in the Flower Garden Banks region, northwestern Gulf of Mexico. In: Coral Reefs of the USA. Springer; 2008. p. 221–61.

32. Johnston MA, Studivan MS, Enochs IC, Correa AMS, Besemer N, Eckert RJ, et al. Coral disease outbreak at the remote Flower Garden Banks, Gulf of Mexico. Front Mar Sci. 2023 Jan 26;10. doi:10.3389/fmars.2023.1111749

33. Tissue Samples Show Coral Disease at Flower Garden Banks is Not Stony Coral Tissue Loss Disease [Internet]. 2024 [cited 2026 Jul 13]. Available from: https://sanctuaries.noaa.gov/notes/2024/coral-disease-at-flower-garden-banks.html

34. Maor-Landaw K, Karako-Lampert S, Ben-Asher HW, Goffredo S, Falini G, Dubinsky Z, et al. Gene expression profiles during short-term heat stress in the red sea coral Stylophora pistillata. Glob Change Biol. 2014;20(10):3026–35. doi:10.1111/gcb.12592

35. Mazzi Esquinca ME, Correa CN, Marques de Barros G, Montenegro H, Mantovani de Castro L. Multiomic Approach for Bioprospection: Investigation of Toxins and Peptides of Brazilian Sea Anemone Bunodosoma caissarum. Mar Drugs. 2023 Mar;21(3):197. doi:10.3390/md21030197

36. Haqshenas G, Doerig C. Targeting of host cell receptor tyrosine kinases by intracellular pathogens. Sci Signal. 2019 Sep 17;12(599):eaau9894. doi:10.1126/scisignal.aau9894

37. Lemmon MA, Schlessinger J. Cell Signaling by Receptor Tyrosine Kinases. Cell. 2010 Jun;141(7):1117–34. doi:10.1016/j.cell.2010.06.011

38. Traylor-Knowles N, Connelly MT, Young BD, Eaton K, Muller EM, Paul VJ, et al. Gene Expression Response to Stony Coral Tissue Loss Disease Transmission in M. cavernosa and O. faveolata From Florida. Front Mar Sci. 2021 Jun 29;8:681563. doi:10.3389/fmars.2021.681563

39. Emery MA, Gutierrez-Andrade D, Changsut I, Swain HL, Fuess LE, Mydlarz LD. Immune System Components in Cnidarians. In: Kaye PM, editor. Encyclopedia of Immunobiology (Second Edition) [Internet]. Second Edition. Oxford: Academic Press; 2026. p. 802–21. Available from: https://www.sciencedirect.com/science/article/pii/B9780128244654001228 doi:https://doi.org/10.1016/B978-0-128-24465-4.00122-8

40. Gorman LM, Tivey TR, Raymond EH, Ashley IA, Oakley CA, Grossman AR, et al. Stability of the cnidarian–dinoflagellate symbiosis is primarily determined by symbiont cell-cycle arrest. Proc Natl Acad Sci. 2025;122(14):e2412396122.

41. Rosset S, Wiedenmann J, Reed AJ, D'Angelo C. Phosphate deficiency promotes coral bleaching and is reflected by the ultrastructure of symbiotic dinoflagellates. Mar Pollut Bull. 2017 May 15;118(1):180–7. doi:10.1016/j.marpolbul.2017.02.044

42. Behrouz ZD, Fahimeh E, Neda S. Dinoflagellate Endosymbiont of the Soft Coral Stichodactyla haddoni Saville-Kent Collected from the Coast of Hormuz Island, Strait of Hormuz. Russ J Mar Biol. 2021 Mar 1;47(2):126–33. doi:10.1134/S1063074021020127

43. Bellantuono AJ, Dougan KE, Granados-Cifuentes C, Rodriguez-Lanetty M. Free-living and symbiotic lifestyles of a thermotolerant coral endosymbiont display profoundly distinct transcriptomes under both stable and heat stress conditions. Mol Ecol. 2019;28(24):5265–81. doi:10.1111/mec.15300

44. Martinez S, Grover R, Ferrier-Pagès C. Symbiont starvation affects the stability of the coral–Symbiodiniaceae symbiosis. Front Mar Sci. 2022 Sep 13;9. doi:10.3389/fmars.2022.979563

45. Oakley CA, Newson GI, Peng L, Davy SK. The Symbiodinium Proteome Response to Thermal and Nutrient Stresses. Plant Cell Physiol. 2022 Dec 24;64(4):433–47. doi:10.1093/pcp/pcac175 PubMed PMID: 36565060; PubMed Central PMCID: PMC10109209.

46. Schmitz G, Müller G. Structure and function of lamellar bodies, lipid-protein complexes involved in storage and secretion of cellular lipids. J Lipid Res. 1991 Oct 1;32(10):1539–70. doi:10.1016/S0022-2275(20)41642-6

47. Stahlman MT, Gray MP, Falconieri MW, Whitsett JA, Weaver TE. Lamellar Body Formation in Normal and Surfactant Protein B-Deficient Fetal Mice. Lab Invest. 2000 Mar 1;80(3):395–403. doi:10.1038/labinvest.3780044

48. Lourdin D, Putaux JL, Potocki-Véronèse G, Chevigny C, Rolland-Sabaté A, Buléon A. Crystalline Structure in Starch. In: Nakamura Y, editor. Starch: Metabolism and Structure [Internet]. Tokyo: Springer Japan; 2015. p. 61–90. Available from: https://doi.org/10.1007/978-4-431-55495-0_3 doi:10.1007/978-4-431-55495-0_3

49. Stephens D, Faghihi Z, Moniruzzaman M. Widespread occurrence and diverse origins of polintoviruses influence lineage-specific genome dynamics in stony corals. Virus Evol. 2024 Oct 17;10(1):veae039. doi:10.1093/ve/veae039

50. Bellas CM, Sommaruga R. Polinton-like viruses are abundant in aquatic ecosystems. Microbiome. 2021 Jan 12;9(1):13. doi:10.1186/s40168-020-00956-0

51. Bulzu PA, Henriques Vieira H, Ghai R. Lineage-specific expansions of polinton-like viruses in photosynthetic cryptophytes. Microbiome. 2025 Jul 1;13(1):154. doi:10.1186/s40168-025-02148-0

52. Pratte ZA, Richardson LL. Microbiome dynamics of two differentially resilient corals. Dis Aquat Organ. 2018 Nov 20;131:213–26. doi:10.3354/dao03289

53. Apprill A, Weber LG, Santoro AE. Distinguishing between Microbial Habitats Unravels Ecological Complexity in Coral Microbiomes. mSystems. 2016 Oct 25;1(5):10.1128/msystems.00143-16. doi:10.1128/msystems.00143-16

54. Bloomberg J, Hutchinson S, Becker C, Meiling S, Bloomberg M, Brandt M, et al. Longitudinal microbiomes of coral and near-coral seawater are influenced by disease phase. Cell Rep Sustain. 2026 Mar 27;3(3). doi:10.1016/j.crsus.2025.100606

55. Ali A, Kriefall NG, Emery LE, Kenkel CD, Matz MV, Davies SW. Recruit symbiosis establishment and Symbiodiniaceae composition influenced by adult corals and reef sediment. Coral Reefs. 2019 Jun 1;38(3):405–15. doi:10.1007/s00338-019-01790-z

56. Karrick CE, Veglia AJ, Meiling S, Maxwell K, Huebner LK, Holstein DM, et al. Key coral symbiont lineages (Family Symbiodiniaceae) are differentially associated with stony coral tissue loss disease (SCTLD). in review.

57. Nguyen-Dinh V, Herker E. Ultrastructural Features of Membranous Replication Organelles Induced by Positive-Stranded RNA Viruses. Cells. 2021 Sep 13;10(9):2407. doi:10.3390/cells10092407

58. Romero-Brey I, Merz A, Chiramel A, Lee JY, Chlanda P, Haselman U, et al. Three-Dimensional Architecture and Biogenesis of Membrane Structures Associated with Hepatitis C Virus Replication. Luo GG, editor. PLoS Pathog. 2012 Dec 6;8(12):e1003056. doi:10.1371/journal.ppat.1003056

59. Donohue ME, Hert ZL, Karrick CE, Rowe AK, Wright PC, Randriamanandaza LJ, et al. Lemur Gut Microeukaryotic Community Variation Is Not Associated with Host Phylogeny, Diet, or Habitat. Microb Ecol. 2023 Oct 1;86(3):2149–60. doi:10.1007/s00248-023-02233-7

60. Sun R, Xu W, Xu Y, Xu Z, Tan Y, Li J, et al. Environmental gradients shape viral-host dynamics in the Pearl River estuary. ISME Commun. 2025 Jan 17;5(1):ycaf164. doi:10.1093/ismeco/ycaf164

61. Yeh YC, Fuhrman JA. Contrasting diversity patterns of prokaryotes and protists over time and depth at the San-Pedro Ocean Time series. ISME Commun. 2022 Dec 1;2(1):36. doi:10.1038/s43705-022-00121-8

62. Vega Thurber R, Correa AMS, Coy S, Veglia A, Fuques E, Hamor C. Meta-transcriptomics to determine if and how viruses are involved in SCTLD infection status and/or disease susceptibility | Florida Department of Environmental Protection [Internet].

2023 [cited 2025 Nov 20]. Available from: https://floridadep.gov/rcp/coral-protection-restoration/documents/meta-transcriptomics-determine-if-and-how-viruses-are-0

63. Veglia AJ. Detecting and Interpreting Viral Dynamics in Marine Invertebrate Holobionts [Ph.D.] [Internet]. [United States -- Texas]: Rice University; 2023 [cited 2025 Nov 20]. Available from: https://www.proquest.com/docview/3089690388/abstract/6168254148574CE4PQ/1

64. Hume BCC, Ziegler M, Poulain J, Pochon X, Romac S, Boissin E, et al. An improved primer set and amplification protocol with increased specificity and sensitivity targeting the Symbiodinium ITS2 region. PeerJ. 2018 May 23;6:e4816. doi:10.7717/peerj.4816

65. Apprill A, McNally S, Parsons R, Weber L. Minor revision to V4 region SSU rRNA 806R gene primer greatly increases detection of SAR11 bacterioplankton. Aquat Microb Ecol. 2015 Jun 4;75:129–37. doi:10.3354/ame01753

66. Parada AE, Needham DM, Fuhrman JA. Every base matters: assessing small subunit rRNA primers for marine microbiomes with mock communities, time series and global field samples. Environ Microbiol. 2015 Aug 14;18(5):1403–14. doi:https://doi.org/10.1111/1462-2920.13023

67. Kozich JJ, Westcott SL, Baxter NT, Highlander SK, Schloss PD. Development of a dual-index sequencing strategy and curation pipeline for analyzing amplicon sequence data on the MiSeq Illumina sequencing platform. Appl Environ Microbiol. 2013;79(17):5112–20.

68. Hume BCC, Smith EG, Ziegler M, Warrington HJM, Burt JA, LaJeunesse TC, et al. SymPortal: A novel analytical framework and platform for coral algal symbiont next-generation sequencing ITS2 profiling. Mol Ecol Resour. 2019 Feb 11;19(4):1063–80. doi:10.1111/1755-0998.13004

69. McMurdie PJ, Holmes S. phyloseq: An R Package for Reproducible Interactive Analysis and Graphics of Microbiome Census Data. PLOS ONE. 2013 Apr 22;8(4):e61217. doi:10.1371/journal.pone.0061217

70. Wickham H. ggplot2: Elegant Graphics for Data Analysis. Springer-Verl N Y [Internet]. 2016. Available from: https://ggplot2.tidyverse.org

71. Callahan BJ, McMurdie PJ, Rosen MJ, Han AW, Johnson AJA, Holmes SP. DADA2: High-resolution sample inference from Illumina amplicon data. Nat Methods. 2016;13(7):581–3.

72. Quast C, Pruesse E, Yilmaz P, Gerken J, Schweer T, Yarza P, et al. The SILVA ribosomal RNA gene database project: improved data processing and web-based tools. Nucleic Acids Res. 2012;41(D1):D590–6.

73. Gloor GB, Macklaim JM, Pawlowsky-Glahn V, Egozcue JJ. Microbiome datasets are compositional: and this is not optional. Front Microbiol. 2017;8:2224.

74. Oksanen J, Simpson GL, Blanchet FG, Kindt R, Legendre P, Minchin PR, et al. vegan: Community Ecology Package [Internet]. 2026. Available from: https://vegandevs.github.io/vegan/

75. Bayer T, Aranda M, Sunagawa S, Yum LK, DeSalvo MK, Lindquist E, et al. Symbiodinium transcriptomes: genome insights into the dinoflagellate symbionts of reef-building corals. PloS One. 2012;7(4):e35269.

76. Parkinson JE, Baumgarten S, Michell CT, Baums IB, LaJeunesse TC, Voolstra CR. Gene expression variation resolves species and individual strains among coral-associated dinoflagellates within the genus Symbiodinium. Genome Biol Evol. 2016;8(3):665–80.

77. Davies SW, Ries JB, Marchetti A, Castillo KD. Symbiodinium functional diversity in the coral Siderastrea siderea is influenced by thermal stress and reef environment, but not ocean acidification. Front Mar Sci. 2018;5:150.

78. Bushnell B. BBMap: A Fast, Accurate, Splice-Aware Aligner [Internet]. 2014 Mar 19 [cited 2026 Feb 27]. Available from: https://escholarship.org/uc/item/1h3515gn

79. Bankevich A, Nurk S, Antipov D, Gurevich AA, Dvorkin M, Kulikov AS, et al. SPAdes: A New Genome Assembly Algorithm and Its Applications to Single-Cell Sequencing. J Comput Biol. 2012 May 1;19(5):455–77. doi:10.1089/cmb.2012.0021

80. Coclet C, Camargo AP, Roux S. MVP: a modular viromics pipeline to identify, filter, cluster, annotate, and bin viruses from metagenomes. mSystems. 2024 Oct;9(10):e00888-24. doi:10.1128/msystems.00888-24

81. Nayfach S, Camargo AP, Schulz F, Eloe-Fadrosh E, Roux S, Kyrpides NC. CheckV assesses the quality and completeness of metagenome-assembled viral genomes. Nat Biotechnol. 2021 May;39(5):578–85. doi:10.1038/s41587-020-00774-7

82. Roux S, Adriaenssens EM, Dutilh BE, Koonin EV, Kropinski AM, Krupovic M, et al. Minimum Information about an Uncultivated Virus Genome (MIUViG). Nat Biotechnol. 2019 Jan;37(1):29–37. doi:10.1038/nbt.4306

83. McMurdie PJ, Holmes S. phyloseq: An R Package for Reproducible Interactive Analysis and Graphics of Microbiome Census Data. PLOS ONE. 2013 Apr 22;8(4):e61217. doi:10.1371/journal.pone.0061217

84. Quinn TP, Richardson MF, Lovell D, Crowley TM. propr: An R-package for Identifying Proportionally Abundant Features Using Compositional Data Analysis. Sci Rep. 2017 Nov 24;7(1):16252. doi:10.1038/s41598-017-16520-0

85. Tackmann J, Matias Rodrigues JF, von Mering C. Rapid Inference of Direct Interactions in Large-Scale Ecological Networks from Heterogeneous Microbial Sequencing Data. Cell Syst. 2019 Sep 25;9(3):286-296.e8. doi:10.1016/j.cels.2019.08.002

86. Bezanson J, Edelman A, Karpinski S, Shah VB. Julia: A Fresh Approach to Numerical Computing. SIAM Rev. 2017 Jan;59(1):65–98. doi:10.1137/141000671

87. Pedersen TL. tidygraph: A Tidy API for Graph Manipulation [Internet]. 2025. Available from: https://CRAN.R-project.org/package=tidygraph

88. Langfelder P, Horvath S. WGCNA: an R package for weighted correlation network analysis. BMC Bioinformatics. 2008;(1):559.

89. Szklarczyk D, Kirsch R, Koutrouli M, Nastou K, Mehryary F, Hachilif R, et al. The STRING database in 2023: protein–protein association networks and functional enrichment analyses for any sequenced genome of interest. Nucleic Acids Res. 2023 Jan 6;51(D1):D638–46. doi:10.1093/nar/gkac1000

90. Wickham H. ggplot2: Elegant Graphics for Data Analysis [Internet]. Springer-Verlag New York; 2016. Available from: https://ggplot2.tidyverse.org

Supplementary Files

This is a list of supplementary files associated with this preprint. Click to download.

- FGBPSTR22S01.pdf
- FGBPSTR22S02.pdf
- FGBPSTR22S03.pdf